9-12-2021

# Isolating Detrital and Diagenetic Signals in Magnetic Susceptibility Records From Methane-Bearing Marine Sediments

Joel E. Johnson
*University of New Hampshire - Main Campus*, joel.johnson@unh.edu

Stephen C. Phillips
*University of New Hampshire*

William C. Clyde
*University of New Hampshire, Durham*, Will.Clyde@unh.edu

Liviu Giosan
*Woods Hole Oceanographic Institution*

Marta E. Torres
*Oregon State University*

## Recommended Citation

Johnson, J. E., Phillips, S. C., Clyde, W. C., Giosan, L., & Torres, M. E., 2021. Isolating detrital and diagenetic signals in magnetic susceptibility records from methane-bearing marine sediments. Geochemistry, Geophysics, Geosystems, 22, e2021GC009867. https://doi.org/10.1029/2021GC009867

# Isolating Detrital and Diagenetic Signals in Magnetic Susceptibility Records From Methane-Bearing Marine Sediments

Joel E. Johnson[1] , Stephen C. Phillips[1,2] , William C. Clyde[1] , Liviu Giosan[3] , and Marta E. Torres[4]

[1]Department of Earth Sciences, University of New Hampshire, Durham, NH, USA, [2]U.S. Geological Survey, Woods Hole, MA, USA, [3]Department of Geology and Geophysics, Woods Hole Oceanographic Institution, Woods Hole, MA, USA, [4]College of Earth, Ocean, and Atmospheric Sciences, Oregon State University, Corvallis, OR, USA

**Abstract** Volume-dependent magnetic susceptibility ($\kappa$) is commonly used for paleoenvironmental reconstructions in both terrestrial and marine sedimentary environments where it reflects a mixed signal between primary deposition and secondary diagenesis. In the marine environment, $\kappa$ is strongly influenced by the abundance of ferrimagnetic minerals regulated by sediment transport processes. Post-depositional alteration by $H_2S$, however, can dissolve titanomagnetite, releasing reactive Fe that promotes pyritization and subsequently decreases $\kappa$. Here, we provide a new approach for isolating the detrital signal in $\kappa$ and identifying intervals of diagenetic alteration of $\kappa$ driven by organoclastic sulfate reduction (OSR) and the anaerobic oxidation of methane (AOM) in methane-bearing marine sediments offshore India. Using the correlation of a heavy mineral proxy from X-ray fluorescence data (Zr/Rb) and $\kappa$ in unaltered sediments, we predict the primary detrital $\kappa$ signal and identify intervals of decreased $\kappa$, which correspond to increased total sulfur content. Our approach is a rapid, high-resolution method that can identify overprinted $\kappa$ resulting from pyritization of titanomagnetite due to $H_2S$ production in marine sediments. In addition, total organic carbon, total sulfur, and authigenic carbonate $\delta^{13}C$ measurements indicate that both OSR and AOM can drive the observed $\kappa$ loss, but AOM drives the greatest decreases in $\kappa$. Overall, our approach can enhance paleoenvironmental reconstructions and provide insight into paleo-positions of the sulfate-methane transition zone, past enhancements of OSR or paleo-methane seepage, and the role of detrital iron oxide minerals on the marine sediment sulfur sink, with consequences influencing the development of chemosynthetic biological communities at methane seeps.

**Plain Language Summary** In continental margin environments, variation in the magnetic susceptibility ($\kappa$) of marine sediments is influenced primarily by the delivery of detrital magnetic minerals from continental erosion and secondarily by diagenetically driven dissolution and/or growth of new magnetic minerals within the sediments. Bulk sediment measurements of $\kappa$ often record a mixed signal from these processes, making it difficult to distinguish the original depositional detrital signal from *in situ* diagenetic effects. Here, we provide a new approach for isolating the detrital signal in $\kappa$ and identifying intervals of diagenetic alteration in methane-bearing marine sediments in the offshore Krishna-Godavari basin, eastern peninsular India. We utilize measurements of $\kappa$, magnetic properties, a heavy mineral proxy (Zr/Rb from X-ray fluorescence), total organic carbon (TOC) and total sulfur (TS), and authigenic carbonate carbon isotopes to determine which portions of the records reflect primary deposition and which reflect diagenesis associated with abundant TOC or abundant methane. Overall, by decoupling the mixed signal of $\kappa$, our approach can allow for improved interpretation of marine sediment sequences globally and has implications for reconstructing the role of detrital magnetic minerals on the marine sediment sulfur cycle and the development of chemosynthetic biological communities at methane seeps.

## 1. Introduction

Volume-dependent magnetic susceptibility ($\kappa$), the magnetic response of bulk sediment to an applied magnetic field, is indicative of relative abundances of paramagnetic, diamagnetic, and ferrimagnetic minerals, and thus is used extensively to reconstruct paleoenvironments, decipher depositional processes, examine changes in sediment provenance, and understand diagenetic processes in terrestrial and marine settings

(Liu et al., 2012; Maxbauer et al., 2016; Roberts, 2015; Verosub & Roberts, 1995). Non-destructive bulk $\kappa$ measurements are obtained rapidly and routinely by scanning sediment cores collected by ocean (e.g., International Ocean Discovery Program, IODP) and continental (e.g., International Continental Scientific Drilling Program, ICDP) scientific drilling programs, where it is used as a major tool for stratigraphic correlation and paleoenvironmental interpretation. Variation in $\kappa$ in marine stratigraphic sequences is influenced by the detrital input and reworking of magnetic minerals, *in situ* biogenic mineral production, and diagenetic alteration of existing iron oxides and/or precipitation of magnetic iron sulfides (Canfield & Berner, 1987; Housen & Musgrave, 1996; Karlin & Levi, 1983; Larrasoaña et al., 2007; Liu et al., 2012; Novosel et al., 2005; Riedinger et al., 2005; Roberts, 2015). Bulk measurements of $\kappa$ often record a mixed signal from these sources and processes (Larrasoaña et al., 2007; Musgrave & Kars, 2016), making it difficult to separate original depositional patterns from secondary effects.

In continental margin sediments the main detrital minerals that drive high $\kappa$ are titanomagnetite ($Fe_3O_4$-$Fe_2TiO_4$ solid solution series from magnetite to ülvospinel), maghemite ($\gamma Fe_2O_3$), hematite ($\alpha Fe_2O_3$), and goethite ($\alpha FeOOH$), with their relative contributions being a function of their geologic provenance and paleoenvironmental conditions (Liu et al., 2012). Shallow sediment diagenesis can affect $\kappa$ via Fe reduction and oxidation (Hepp et al., 2009; Kasten et al., 1998; Rowan & Roberts, 2006). In addition, ferrimagnetic minerals are subject to reaction with hydrogen sulfide produced during organoclastic sulfate reduction (OSR) ($SO_4 + 2CH_2O \rightarrow H_2S + 2HCO_3^-$), and anaerobic oxidation of methane (AOM) ($SO_4 + CH_4 \rightarrow HS^- + HCO_3^- + H_2O$). AOM occurs at the sulfate-methane transition zone (SMTZ) and is mediated by a bacterial-archeal consortium (Barnes & Goldberg, 1976; Boetius et al., 2000; Hinrichs et al., 1999). Both OSR and AOM produce $HS^-$ and $HCO_3^-$, which can contribute to the precipitation of authigenic carbonate and sulfide minerals in the sediments (e.g. Berner, 1970, 1984; Lin et al., 2016; Passier et al., 1996; Riedinger et al., 2005; Ritger et al., 1987). These secondary authigenic precipitates may remain in the sediments as a wake of mineralization long after the migration of the diagenetic fronts that produced them.

Reduction of existing primary magnetic mineral phases and/or the precipitation of secondary magnetic minerals during diagenesis can alter the primary $\kappa$ signal. The common magnetic detrital iron oxides (magnetite and hematite) react with $H_2S$ on the order of days to hundreds of years (Poulton et al., 2004) and reaction of sufficient $H_2S$ with iron oxides can result in the formation of pyrite ($FeS_2$) (Berner, 1970, 1984), which is paramagnetic. In addition to full pyritization, greigite ($Fe_3S_4$) and pyrrhotite ($Fe_7S_8$) can precipitate as intermediate, magnetic mineral phases and have been documented in methane-bearing marine sediments (Housen & Musgrave, 1996; Kars & Kodama, 2015; Larrasoaña et al., 2007).

A close association between zones of reduced $\kappa$ and the modern SMTZ has been widely documented in marine sediments (e.g., Dewangan et al., 2013; März et al., 2008; Novosel et al., 2005; Riedinger et al., 2005, 2019). Intervals of reduced $\kappa$ in sediment records have also been attributed to increases in sulfide mineral content or total organic carbon (TOC), suggesting a link between non-steady state diagenesis and sedimentation rate, fluid flow, or primary productivity (Badesab et al., 2017; Chang et al., 2016; Hepp et al., 2009; Kars et al., 2017). Zones of reduced $\kappa$ in marine sequences can indicate the evolution of a variable SMTZ driven by changes in the flux of methane from depth, changes in sedimentation rate, or both. A robust assessment of $\kappa$ drawdowns as indicators of paleo-environmental conditions remains difficult, however, due to the mixed nature of the $\kappa$ signal. The first step needed to improve the applicability of $\kappa$ is the development of a method that clearly separates detrital and diagenetic signals in $\kappa$ records; such an approach will be of value for reconstructing paleoenvironmental change and diagenetic processes.

In this paper, we present an approach to isolate the detrital and diagenetic signals in $\kappa$ records at two drill sites drilled in the Krishna-Godavari basin, on the eastern continental margin of India: NGHP-01-10 (Site 10) and NGHP-01-16 (Site 16) (Figure 1; Collett et al., 2015). In addition to measurement of $\kappa$, methane-bearing sediments at these sites were also characterized by measurements of magnetic properties (magnetic susceptibility, isothermal remanent magnetism, thermal demagnetization), X-ray fluorescence (XRF) bulk elemental composition, total organic carbon (TOC), total sulfur (TS), authigenic carbonate $\delta^{13}C$, and with estimates for titanomagnetite and pyrite iron. Collectively, these data are used to model the original detrital $\kappa$ record and isolate the diagenetic effects on $\kappa$ that are driven by OSR and AOM. Continental margins typically have high sedimentation rates that allow for high-resolution stratigraphic records. These regions are also characterized by widespread distribution of magnetic iron oxides and enough organic matter to sustain
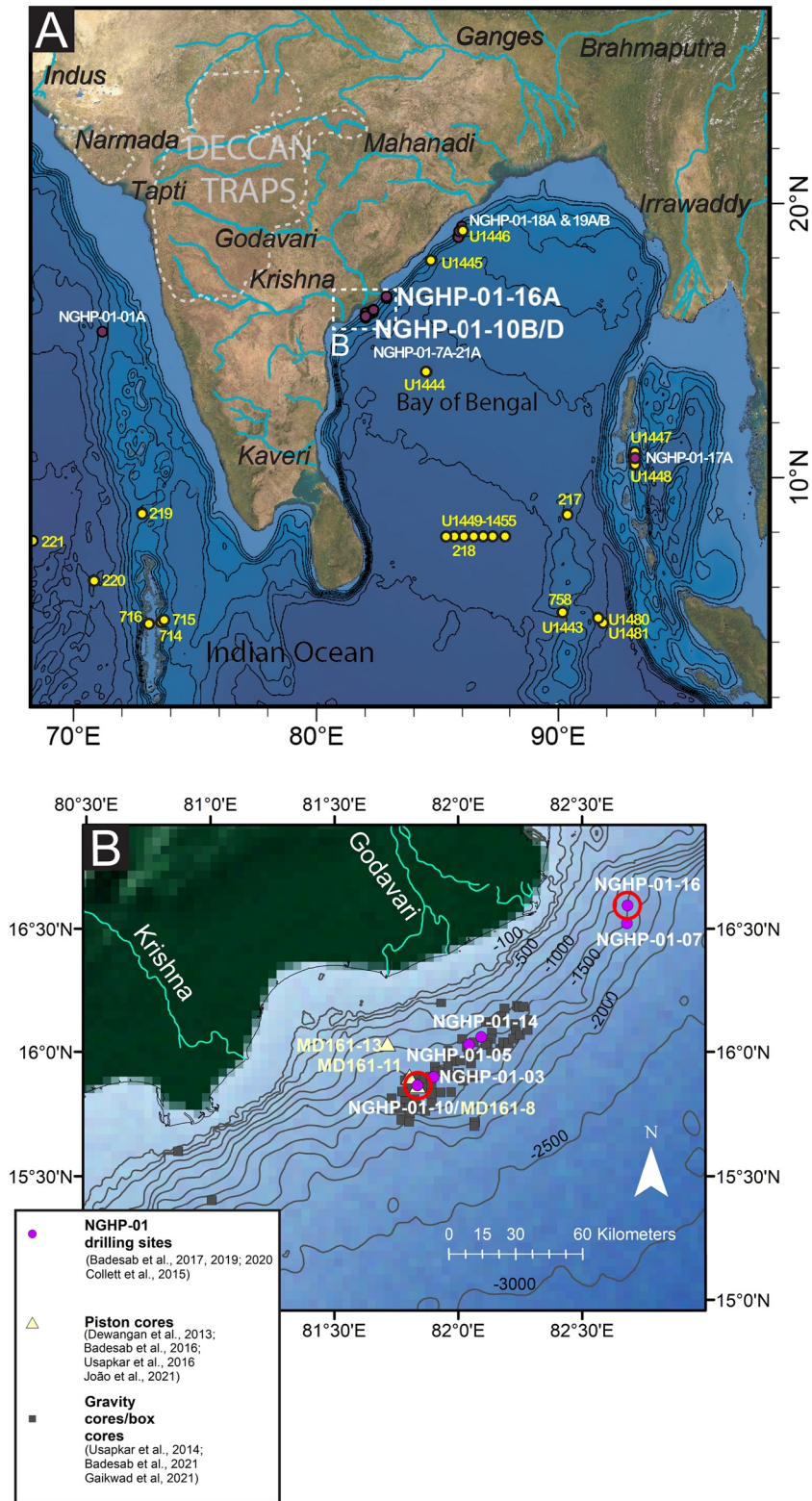
**Figure 1.**

OSR, methane generation, AOM, and gas hydrate accumulations. Therefore, the approach described here is broadly applicable in many continental margin settings. By isolating the detrital and diagenetic components in κ, we can now reconstruct primary mineral fluxes as well as track the effects of OSR, AOM, and the degree of pyritization on magnetic susceptibility. At locations where the SMTZ is sufficiently shallow, the reconstructed diagenetic κ records provide useful information on SMTZ fluctuations that can be used to infer paleo-methane seepage and the near seafloor $H_2S$ availability for chemosynthetic biological communities.

## 2. Geologic Setting

The Krishna-Godavari Basin is one of five pericratonic basins along the eastern Indian margin that formed during the Late Jurassic rifting of the Indian and Australia-Antarctic plates (Powell et al., 1988). The sediments deposited in the offshore Krishna-Godavari Basin are sourced from the Krishna and Godavari Rivers, which drain the Deccan Traps, Dharwar and Bastar cratons, and rocks of the Godavari graben and Eastern Ghats belt, all of which contain possible source rocks for detrital, magnetic iron oxides (e.g. in mafic volcanics, Fe-rich schists, iron formations) (Biksham & Subramanian, 1988; Mazumdar et al., 2015; Mazumder & Eriksson, 2015). The Krishna and Godavari Rivers discharge a combined $174 \times 10^6$ tons of sediment per year, primarily during the summer monsoon season (Biksham & Subramanian, 1988; Ramesh & Subramanian, 1988; Subramanain, 1979) and the Godavari River is among the top 15 largest river sediment discharges in the world (Milliman & Meade, 1983). This sediment discharge is dominated by smectite group clays with minor quartz, feldspar, and kaolinite (Subramanian, 1980). Weathering and sediment transport within the Krishna-Godavari Basin is strongly influenced by monsoon rainfall (Giosan et al., 2017; Kale, 2007; Peketi et al., 2020). The South Asian monsoon has a fundamental impact on continental margin sediment accumulation in Bay of Bengal (e.g., Clemens et al., 2021; Colin et al., 1998; Weber et al., 2018). Thus, the eastern Indian continental margin acts as a supply dominated margin that is most active during interglacial periods of intense monsoon-driven weathering, rather than being sea level controlled (Phillips, Johnson, Giosan, & Rose, 2014). Differential accumulation of sediments through time in the offshore Krishna-Godavari Basin has resulted in shale diapirism (Anitha et al., 2014; Choudhuri et al., 2010), which can change the petroleum system, fluid flow, and gas hydrate system within the basin (Badesab et al., 2017; Dewangan et al., 2010; Joshi et al., 2014; Mandal et al., 2014; Rao, 2001).

Slumping, debris flows, and turbidites are common within the offshore Krishna-Godavari Basin (Collett et al., 2015; Ramprasad et al., 2011) resulting in non-steady state sedimentation (Hong et al., 2014). The Krishna-Godavari Basin contains sufficient TOC for OSR and methanogenesis (Johnson et al., 2014; Peketi et al., 2015) that, coupled with AOM and silicate weathering (Solomon et al., 2014), provides excess alkalinity for authigenic carbonate (Teichert et al., 2014) and Fe-sulfide (Peketi et al., 2015) precipitation. There is widespread evidence for gas hydrate from seismic profiles within the Krishna-Godavari Basin (Jaiswal et al., 2012; Ramana et al., 2009; Shukla, Collett, et al., 2019; Shukla, Kumar, et al., 2019), and fracture-filling gas hydrate was recovered and/or inferred in multiple holes in this basin during NGHP-01 coring and logging on the *D/V JOIDES Resolution* (Collett et al., 2015; Cook et al., 2014; Holland & Schultheiss, 2014; Jaiswal et al., 2014; Rees et al., 2011; Shankar & Riedel, 2014; Stern & Lorenson, 2014). The second NGHP Expedition (NGHP-02), which occurred in 2015, also discovered, characterized, and sampled high-saturation, coarse-grained gas hydrate reservoirs in the Krishna-Godavari Basin (Boswell et al., 2019; Collett et al., 2019; Pandey et al., 2019). Methane within the hydrate stability zone of the Krishna-Godavari Basin is dominantly microbial in origin (Dixit et al., 2019; Lorenson & Collett, 2018; Mazumdar et al., 2012).

Titanomagnetite is the dominant detrital magnetic mineral observed in offshore Krishna-Godavari Basin sedimentary records along with minor titanohematite and goethite (Badesab et al., 2017, 2019, 2020; Dewangan et al., 2013; João et al., 2021; Usapkar et al., 2014). This titanomagnetite is likely sourced from the

**Figure 1.** (a) NGHP-01 Core Sites (purple) on the Indian continental margins. Sites 16 and 10 are located in the Krishna-Godavari Basin. Yellow circles are existing Deep Sea Drilling Project (DSDP), Ocean Drilling Program (ODP) and International Ocean Discovery Program (IODP) sites. Major rivers labeled in black. Inset (b) shows all sites in the offshore Krishna-Godavari Basin with published rock magnetic analyses that document titanomagnetite as the dominant detrital magnetic mineral throughout basin with variable alteration to iron sulfides. Other NGHP drill sites (Sites 03, 05, 10, and 14) have been measured for various rock magnetic properties (Badesab et al., 2017, 2019), as well as piston cores (Badesab et al., 2017; Dewangan et al., 2013; João et al., 2021; Usapkar et al., 2016) and gravity/box cores (Badesab et al., 2021; Usapkar et al., 2014).

Deccan basalts (Banerjee & Mondal, 2021; Bose, 1972; Schöbel & de Wall, 2014), and transported to the Bay of Bengal via the Krishna and Godavari Rivers (Kulkarni et al., 2014, 2015; Sangode et al., 2007). Titanomagnetite content is substantially higher offshore the Krishna and Godavari Rivers compared to the Mahanadi River, which has a catchment less influenced by Deccan basalts (Badesab et al., 2021). The offshore Krishna-Godavari sedimentary records (Figure 1) typically include intervals with evidence of titanomagnetite dissolution and precipitation of pyrite and/or magnetic iron sulfides (Badesab et al., 2017, 2019, 2020; Dewangan et al., 2013; João et al., 2021; Usapkar et al., 2014) suggesting that diagenetic alteration of the primary magnetic mineral assemblage is common. Intervals of low κ are common in NGHP-01 sites throughout the Krishna-Godavari Basin and they often correspond with the modern SMTZ (Collett et al., 2015).

NGHP-01 Site 16 (16° 35.5986' N, 082°41.0070' E) is located on the continental slope in 1,253 m of water depth within the Krishna-Godavari Basin (Figure 1). One lithostratigraphic unit was recovered and defined at this site and includes clay, silty clay, and nannofossil-bearing-to-rich clay, and foraminifer-bearing clay (Collett et al., 2015, Figure 2). Numerous thin silt beds and laminations were observed at this site. Limited calcareous nannofossil and foraminifera biostratigraphic datums suggests the recovered sediments at Site 16 within the Krishna-Godavari Basin are most likely Quaternary (∼1.5 Ma) to recent in age (Flores et al., 2014). Methane hydrate at Site 16 was present only in low saturations as disseminated hydrate inferred from pressure cores, well logs, and rare instances of infrared and chloride anomalies (Collett et al., 2015). The clay mineralogy at Site 16 is primarily smectite group minerals (34%–72%) with substantial illite (14%–30%) and kaolinite (10%–33%) content (Phillips, Johnson, Underwood, et al., 2014). Total organic carbon (TOC) ranges from 0.41 to 2.53 wt.% and $CaCO_3$ ranges from 0 to 23 wt%, with the highest values of TOC and $CaCO_3$ occurring within the upper 35 m below seafloor (mbsf) (Johnson et al., 2014).

At Site 16 whole-round measured shipboard κ (Collett et al., 2015) varies between 16 and 179 SI x $10^{-6}$ (mean 83 SI x $10^{-6}$) in the upper 29.3 mbsf (Figure 2). Between 29.3 and 35.5 mbsf, κ is consistently very low, between 16 and 21 SI x $10^{-6}$ (mean: 18.3 SI x $10^{-6}$). Below 35.5 mbsf, κ shifts abruptly to dramatically higher values in the underlying remainder of the hole to 218 mbsf, ranging from 20 to 576 SI x $10^{-6}$ (mean: 224 SI x $10^{-6}$).

NGHP-01 Site 10 (15° 51.8609' N, 81° 50.0749' E) is located on the continental slope in 1,038 m of water depth in the Krishna-Godavari Basin (Figure 1) and consists of one lithostratigraphic unit of nannofossil- and foraminifer-bearing to rich clay and silty clay (Collett et al., 2015) (Figure 2). The clay is primarily smectite group (42%–84%) with notable illite (0%–26%) and kaolinite (6%–29%) clay minerals (Phillips, Johnson, Underwood, et al., 2014). Median grain size (d0.5) measured by laser diffraction ranges from 4 to 8 μm (over the upper 27 mbsf; discussed in this paper). TOC ranges from 0.6 and 2.4 wt% and $CaCO_3$ varies from 0 to 14 wt% (Johnson et al., 2014). Limited calcareous nannofossil and foraminifera datums suggests the recovered sediments at Site 10 are younger than Late Pliocene (Flores et al., 2014). Methane hydrate was observed at this site in high saturations as veins within fractures, sampled by pressure cores or inferred from well logs, mousse-like textures, or chloride anomalies (Collett et al., 2015; Cook et al., 2014; Holland & Schultheiss, 2014; Rees et al., 2011). Bivalve, worm tube, and barnacle fossils, as well as authigenic carbonate nodules between 16 and 20 mbsf are vestiges of a Pleistocene paleo-seep community that existed from ∼42 to 53 ka (Collett et al., 2015; Gale et al., 2020; Mazumdar et al., 2009). In addition, a Mo and δ$^{34}$S anomaly from this interval provide additional evidence for paleo-methane and $H_2S$ venting (Peketi et al., 2012). The first modern seafloor chemosynthetic community in the Krishna-Godavari Basin was recently identified at an active methane seep in ∼1,750 m water depth (Mazumdar et al., 2019), down slope from our study sites.

At Site 10 whole-round measured shipboard κ (Collett et al., 2015) throughout the upper 27 mbsf ranges from 15 to 176 SI x $10^{-6}$ (Figure 2). κ is relatively high over the upper 8.5 mbsf ranging between 116 and 160 SI x $10^{-6}$. κ is very low and consistently ranges between 21 and 41 SI x $10^{-6}$ in the intervals 8.5 and 17 mbsf and 23 and 27 mbsf. Between 17 and 23 mbsf, κ increases to 37 to 176 SI x $10^{-6}$. In a companion piston core (MD-161) near Site 10, the primary magnetic mineral was identified as titanomagnetite by rock magnetic, electron microscopy, and X-ray diffraction measurements, with an interval containing greigite between 17 and 23 msbf (Dewangan et al., 2013). The low κ and greigite-bearing intervals correspond to high chromium reducible sulfur (CRS) (0.5–3.7 wt%) (Dewangan et al., 2013). Overall, at Site 10 there is a negative correlation between magnetite concentration and CRS suggesting that $H_2S$ related diagenesis driven by changes in methane flux has altered the κ signal (Badesab et al., 2017).
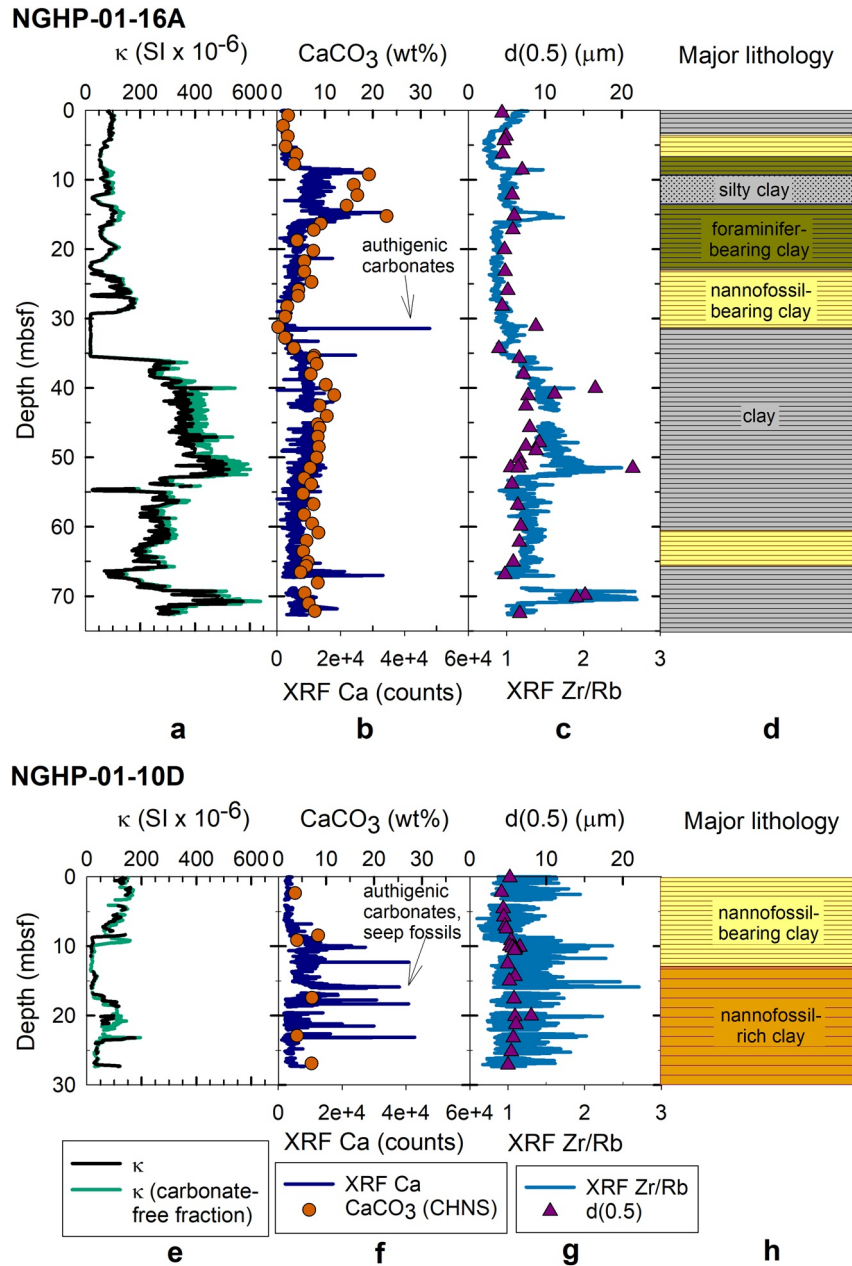
**Figure 2.** Stratigraphic context of NGHP-01 Site 16 Hole A and Site 10 Hole D. (a and e) κ and κ corrected for the carbonate-free fraction. (b and f) $CaCO_3$ measured by CHNS and Ca measured by XRF. (c and g) Median grain size (d(0.5)) from laser diffraction particle size analysis and Zr/Rb from XRF. (d and h) Major lithology from visual and smear slide description (Collett et al., 2015).

# 3. Materials and Methods

## 3.1. Overall Approach

Identification of the detrital and diagenetic minerals responsible for the κ signal in a sedimentary record can be achieved through rock magnetic, mineralogical, or geochemical approaches; however, in long sedimentary records obtained through ocean and continental drilling these approaches can be very labor-intensive, resulting in a limitation in down core resolution. Here we describe a new approach that takes advantage of routine high-resolution magnetic and sediment geochemical data to deconvolve the detrital and diagenetic signals in κ records collected in methane-bearing sediments along continental margins.

We utilize Zr/Rb elemental ratios from XRF core scanning as a proxy for the detrital heavy mineral content of the sediments, which is highly correlated with κ along the eastern margin of peninsular India (Phillips, Johnson, Giosan, & Rose, 2014). Zr/Rb has been used as a grain size proxy (e.g., Chen et al., 2006; Dypvik & Harris, 2001; Gebregiorgis et al., 2020; Toyos et al., 2020) due to the enrichment of Zr in sediment coarse fractions. However, the relationships between Zr/Rb and grain size is not always consistent in marine sediments, especially in fine-grained sediments with limited coarse, detrital fraction (Phillips, Johnson, Giosan, & Rose, 2014; Wu et al., 2020). For example, in the sites studied here, we observe good agreement between Zr/Rb and measured grain size at Site 16, a relatively coarser record, but less so at Site 10, which a finer grained record (Figure 2). Fundamentally, Zr/Rb is a heavy mineral proxy corresponding to the ratio of Zr present in resistant, detrital zircon grains and Rb that is dispersed in the clay minerals. Magnetic susceptibility is dependent on particle size (Hatfield et al., 2017, 2019; Razik et al., 2014), and the general dependence on grain size for κ and Zr/Rb may explain their correlation.

Due to similar high grain densities of zircon (4.669 g cm$^{-3}$) and titanomagnetite (4.776–5.200 g cm$^{-3}$) (Johnson & Olhoeft, 1984) relative to the grain density of the background sediments (2.72 g cm$^{-3}$) (Collett et al., 2015), we suspect these minerals experienced similar sediment transport and depositional histories in the cores examined for this study. Thus, in the absence of diagenesis and assuming no major shifts in provenance, the Zr/Rb ratio (zircon) and κ (titanomagnetite) should have similar downcore patterns, as observed by Phillips, Johnson, Giosan, and Rose (2014). The downcore detrital pattern inferred from Zr/Rb is compared to the κ pattern to identify intervals of altered κ, which we interpret to be indicative of a diagenetic overprint.

We constrain this interpretation by tracking diagenetic mineral reactions, as preserved in the solid phase products, through measurements of magnetic mineral assemblages, TS and TOC, and δ$^{13}$C of authigenic carbonates. Our results show multiple diagenetic drawdowns in κ preserved in these records, and we attribute these signals to diagenetic alteration of titanomagnetite by H$_2$S produced from OSR and AOM. Portions of our κ records that are not depleted relative to Zr/Rb, can be attributed to a primary κ driven by detrital mineral fluxes.

### 3.2. Magnetic Susceptibility and Isothermal Remanent Magnetism

Volume-normalized magnetic susceptibility (κ, SI x 10$^{-6}$) was measured on whole-round sections using a Geotek multi-sensor core logger (MSCL) on board the *D/V JOIDES Resolution* (Collett et al., 2015). Discrete samples ($n = 37$) were collected in 8 cm$^3$ cubes and stored at ~4 C. 1 cm$^3$ subsamples were measured for mass-dependent magnetic susceptibility (χ, m$^3$ kg$^{-1}$) and compare well to the shipboard volume normalized κ measurements (Figure S1), suggesting minimal alteration post-sampling. We also calculated a carbonate-free κ by adjusting the measured κ based on CaCO$_3$ wt% and XRF Ca counts (Figures 2 and S2). Isothermal remanent magnetization (IRM) with 3-axis thermal demagnetization was performed on 22, 1 cm$^3$ samples (Site 10) and 15, 1 cm$^3$ samples (Site 16) at the University of New Hampshire Paleomagnetism Laboratory. χ was measured using a Bartington MS2 magnetic susceptibility meter. IRM was measured using an HSM2 SQUID spinner magnetometer. IRM was applied in 16 steps between 0 to 1,100 mT using an ASC IM-10 impulse magnetizer. After imparting the 1,100 mT field along the primary axis, fields of 400 and 120 mT were imparted at right angles to the primary axis (Lowrie, 1990). We refer to the 1,100, 400, and 120 mT as the hard, medium and soft axis, respectively. Samples were thermally demagnetized from room temperature to 680°C over 21 steps using an ASC TD48-SC magnetically shielded oven, measuring the magnetization along each axis after each step (Lowrie, 1990). We characterized magnetic mineral assemblages from the combination of IRM acquisition and thermal demagnetization curves. From the IRM acquisition curves we calculated the saturation IRM (SIRM) and the field at which half of SIRM is reached (B$_{1/2}$) using the approach of Kruiver et al. (2001).

### 3.3. X-Ray Fluorescence

XRF core scanning was performed using a Cox Analytical XRF core scanner at Woods Hole Oceanographic Institution (WHOI) on split core surfaces. Zr, Rb, Fe, Ti, and K in these cores were measured every 4 mm down core for 20 s at each step with a 30 mA/60 kV energy level.

### 3.4. CHNS Elemental Analysis

Samples were dried in an oven at 40°C and powdered, and then measured on a Perkin Elmer CHNS/O 2400 Series II elemental analyzer. Bulk, untreated samples were run for total carbon (TC), total nitrogen (TN), and total sulfur (TS). Total organic carbon (TOC) was measured on samples treated with 6% sulfurous acid using the method described in Phillips et al. (2011). Replicates were run approximately every 10 samples with a precision of 0.08, 0.01, and 0.03 wt% for TC, TN, and TS respectively. Soil standards from Elemental Microanalysis were also run approximately every 10 samples with an accuracy of 0.03, 0.02, and 0.03 wt% for TC, TN, and TS respectively.

### 3.5. Age Model

Age models at Site 10 and Site 16 were derived from published radiocarbon-based ages (Mazumdar et al., 2009; Ponton et al., 2012). We expanded age assignments at Site 16 with additional radiocarbon and benthic $\delta^{18}O$ data. For our radiocarbon ages, we picked mixed plankic foraminifers (primarily *Globigerinoides ruber* and *Globigerinoides sacculifer*) for three samples at 10.05, 11.05, and 12.55 mbsf. These samples were measured at the National Ocean Sciences Accelerator Mass Spectrometry (NOSAMS) facility at Woods Hole Oceanographic Institution (WHOI), using the $H_3PO_4$ hydrolysis method. Radiocarbon ages were calibrated to calendar ages with CALIB 8.2 software (Stuiver et al., 2021) and the Marine20 calibration curve (Heaton et al., 2020). The standard marine reservoir correction of 400 years was used for calibration, and this value is bracketed by the two nearest reservoir corrections in the Bay of Bengal (Dutta et al., 2001; Southon et al., 2002).

The age model was expanded by oxygen isotope measurements of benthic foraminifers *Uvigerina peregrina* and *Hoeglundina elegans*. From these two $\delta^{18}O$ series, multiple oxygen isotope events were identifiable based on the chronology of Imbrie et al. (1984) and Lisiecki and Raymo (2005) (see Figure S3). $\delta^{13}C$ and $\delta^{18}O$ data are expressed relative to the Vienna Pee Dee Belemnite (VPDB) standard as ‰. Foraminfer abundance was too low below 40 mbsf to be able to measure stable isotopes and the $\delta^{18}O$ was uninterpretable below 25 mbsf, possibly due to diagenetic overprint as suggested by light $\delta^{13}C$ isotopes (Figure S3).

### 3.6. Authigenic Carbonate Isotopes and Mineralogy

Authigenic nodules from NGHP-01 sites were previously analyzed by Teichert et al. (2014), however, the upper 110 mbsf from Site 16 were not sampled at sea and thus not included in their study. We analyzed nodules sampled from the upper 73 mbsf from Site 16 for $\delta^{13}C$ and $\delta^{18}O$ analysis and X-ray diffraction (XRD) to supplement the authigenic carbonate analyses on deeper samples at this site by Teichert et al. (2014). Authigenic carbonate $\delta^{13}C$ and $\delta^{18}O$ from Site 10 was measured to supplement the analyses from Mazumdar et al. (2009) and Teichert et al. (2014). Carbonate nodules were dried, crushed, and stored in glass vials prior to analysis. Carbonates from Site 10 were measured at the Oregon State University Stable Isotope Laboratory with a Finnigan MAT 252 mass spectrometer with a Kiel III carbonate preparation device (phosphoric acid at 70°C). Carbonates from Site 16 were measured at the University of Michigan Stable Isotope Laboratory with a Finnigan MAT 253 mass spectrometer with a Kiel IV carbonate preparation device (phosphoric acid at 77 °C). $\delta^{13}C$ and $\delta^{18}O$ data are expressed relative to the VPDB as ‰. Both mass spectrometers were calibrated by NBS 19 standards: University of Michigan average and standard deviation was $\delta^{13}C = 1.94 \pm 0.07$ and $\delta^{18}O = -2.25 \pm 0.07$, and Oregon State University was $\delta^{13}C = 1.89 \pm 0.1$ and $\delta^{18}O = -2.16 \pm 0.08$.

Powdered samples from Site 16 were analyzed using a Siemens D5000 X-ray Diffractometer and Kristalloflex 710 X-ray generator at the University of New Hampshire. The XRD was operated with source energy of 40 kV and 30 mA, a divergence slit of 2 mm, and receiving/scatter slits of 2, 0.05, and 0.5 mm. Samples were measured over a 2Θ range from 10° to 40° at a step of 0.04° 2Θ, with 20 s measurements at each step. Diffractograms were analyzed using Bruker-AXS EVA and International Centre for Diffraction Data (ICDD) database to calculate peaks and identify minerals.
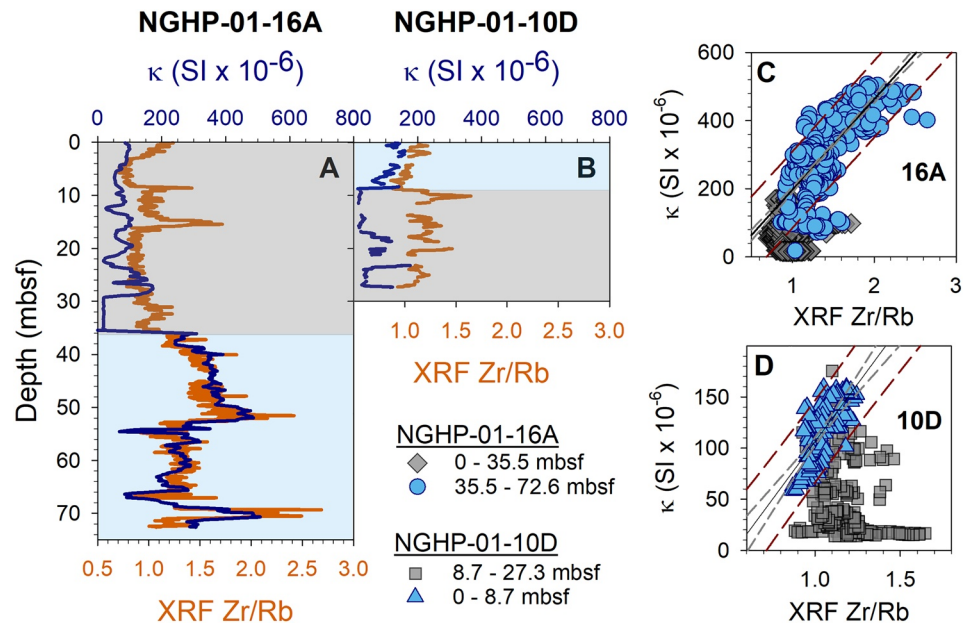
**Figure 3.** Comparison of κ and the XRF-derived Zr/Rb heavy mineral proxy at Site 16 and 10 (a and b). κ and Zr/Rb correlation with 95% confidence (gray dashed lines) and prediction intervals (red dashed lines) for Site 16 (35–73 mbsf) and Site 10 (0–9 msbf) (c and d). Blue shading in A and B show the coupled intervals of Zr/Rb and κ used for the regression in (c and d). Gray shading highlights intervals in which Zr/Rb and κ are decoupled.

### 3.7. Prediction of Primary Detrital Titanomagnetite

Intervals in which κ and XRF Zr/Rb are well correlated are inferred to reflect a primary detrital κ signal associated with depositional processes, as has been observed elsewhere on the eastern Indian margin (Phillips, Johnson, Giosan, & Rose, 2014). Good correlation ($R^2 = 0.60$ at Site 16 and 0.51 at Site 10) between κ and Zr/Rb was observed between 35 and 73 mbsf at Site 16 and between 0 and 9 mbsf at Site 10 (Figure 3). Predictions of primary detrital κ were made by linear regression of κ and Zr/Rb in these intervals and this best-fit relationship was extrapolated over the entire record of available XRF data (0–73 mbsf at Site 16 and 0–28 mbsf at Site 10). The 95% prediction limits, used to assign upper and lower bounds to the predicted detrital signal, were derived using SigmaPlot 11.0 software.

### 3.8. Calculation of Predicted Titanomagnetite Loss and Pyrite Gain

The loss of κ was calculated by subtraction of measured κ values from predicted κ based on Zr/Rb data. This difference was then converted into an estimate of titanomagnetite loss based on a titanomagnetite-dominated assemblage, as indicated by the IRM and 3-axis thermal demagnetization data (see Section 4). Assuming the loss of κ is driven by complete dissolution of titanomagnetite and precipitation of pyrite (all titanomagnetite Fe released by reaction with $H_2S$ is ultimately bound as $FeS_2$), 1.15 wt% of pyrite sulfur will be precipitated for every 1 wt% of titanomagnetite Fe reduced. Because we do not know the exact titanomagnetite composition, we considered a range in κ values along the titanomagnetite series for this estimation. Along the titanomagnetite series, variation in Ti compositions can result in ranges in κ from 4,800 (ülvospinel) to 5,700,000 (magnetite) (Hunt et al., 1995) resulting in drastically different predictions of titanomagnetite loss and pyrite precipitation (Figure S4). In Figure 6 we show predicted pyrite S based on titanomagnetite κ of 130,000 SI x $10^{-6}$ SI, which corresponds to an intermediate titanomagnetite composition of $Fe_{2.4}Ti_{0.6}O_4$ (TM60) (Hunt et al., 1995 and Figure S2). TM60 is consistent with the composition of Deccan basalt (Radhakrishnamurty & Subbrao, 1990), the dominant source terrane for titanomagnetite in the Krishna-Godavari Basin.

## 4. Results

### 4.1. Reconstructing Detrital Magnetic Susceptibility

To decipher the detrital κ mineral carrier, we measured IRM acquisition and thermal demagnetization curves of sediments from Sites 10 and 16. Overall, our IRM results show a low coercivity assemblage with a loss of nearly all magnetization by 575°C, indicating that titanomagnetite is the dominant primary detrital magnetic mineral at both sites (Figures 4 and 5). Samples between 0 and 8.5 mbsf at Site 10 and 36 to 73 mbsf at Site 16 (intervals of high κ) show a dominant low-coercivity ferrimagnetic component with very little contribution from high coercivity magnetic minerals (Figure 4). Within these intervals of high κ, IRM reaches >90% of the IRM at 1.1T by 0.11T; $B_{1/2}$ is consistently <40 mT (Figures 4a and 4b). During thermal demagnetization, the magnetization is dominantly along the soft axis and decreases to 575°C with a change in slope at ~325–350°C (Figures 4a and 4b). In intervals of low κ (e.g., 29–35 mbsf at Site 16 and 11–16 mbsf at Site 10), SIRM is lower and $B_{1/2}$ increases, indicating a higher concentration of high-coercivity components. Within these intervals of low κ, IRM only reaches 46%–66% of the IRM at 1.1T by 0.11T; $B_{1/2}$ is higher at 56–126 mT (Figures 4c and 4d). During thermal demagnetization, the magnetization along the medium and hard axis typically exceeds or is approximately equal to the soft axis, retaining some magnetization to 675°C. This suggests that the primary low-coercivity titanomagnetite has been subject to major dissolution, leaving more resistant, higher coercivity magnetic minerals (Garming et al., 2005; Poulton et al., 2004). At Site 10, we observe properties consistent with the presence of greigite between 17 and 23 mbsf, consistent with previously measured properties by Dewangan et al. (2013). IRM acquisition curves in this interval are similar to other high κ intervals but with demagnetization curves where IRM along the soft axis is lost by ~350°C consistent with the unblocking temperature of greigite.

Our IRM and thermal demagnetization results are consistent with the extensive work of Badesab et al. (2017, 2019, 2020), Dewangan et al. (2013), Gaikwad et al. (2021), João et al. (2021), and Usapkar et al. (2014) who used IRM and additional rock magnetic parameters (e.g., anhysteric remanent magnetization (ARM), and S-ratio) coupled with XRD and SEM EDS to document a dominant presence of titanomagnetite and minor amounts of hematite and goethite in the magnetic assemblages of the Krishna-Godavari Basin, with distinct intervals bearing magnetic iron sulfides and pyrite as diagenetic overprints. These comprehensive rock magnetic studies include Site MD-161 (Dewangan et al., 2013) which is about 100 m from NGHP-01 Site 10, and NGHP-01 Site 07 (Badesab et al., 2019), which is 8 km to the south of NGHP-01 Site 16. The consistency of the primary magnetic mineral assemblage dominated by titanomagnetite across the Krishna-Godavari Basin as determined from five NGHP-01 sites, including the same sites as or nearby sites to those in this study, give confidence in our interpretation of the magnetic mineral assemblage from IRM and thermal demagnetization. These studies document losses in fine-grained titanomagnetite, precipitation of pyrite and greigite/pyrrhotite, and relative increases in high-coercivity minerals in zones affected by $H_2S$-related diagenesis. In addition, numerous gravity cores collected throughout the KG-Basin show titanomagnetite with reduced magnetic susceptibility or greigite presence at seep sites (Gaikwad et al., 2021; Usapkar et al., 2014).

Based on room temperature property measurements (Peters & Dekkers, 2003) all of our samples except one plot as titanomagnetite-dominant (Figure 5). Samples with lower total S tend to plot toward the higher SIRM/χ range (closer to magnetic iron sulfides) and samples with higher total S tend to plot toward the lower SIRM/χ and higher $B_{1/2}$ range (closer to hematite and goethite).

Due to gravity sorting during deposition, titanomagnetite series minerals in marine sediments are commonly deposited with other heavy minerals, which we track using XRF Zr/Rb measurements on split core surfaces. Comparing the Zr/Rb and κ records at Site 16, we see a good correlation between 36 and 73 mbsf whereas sediment between 0 to 36 mbsf is not well correlated (Figure 3). At Site 10, a good correlation is observed between 0 and 8 mbsf, but no correlation is apparent from 8 to 27 mbsf. We argue that portions of the records where κ tracks the Zr/Rb heavy mineral proxy, reflect the magnetic signal from a detrital titanomagnetite flux. In contrast, relative variations in κ that are decoupled from the Zr/Rb heavy mineral proxy likely represent zones where either titanomagnetite deposition decreases relative to zircon or the original detrital κ has been altered by diagenesis. We estimate an equivalent titanomagnetite loss by subtracting the measured κ signal from a Zr/Rb-derived detrital κ profile. If we assume complete pyritization, our estimated
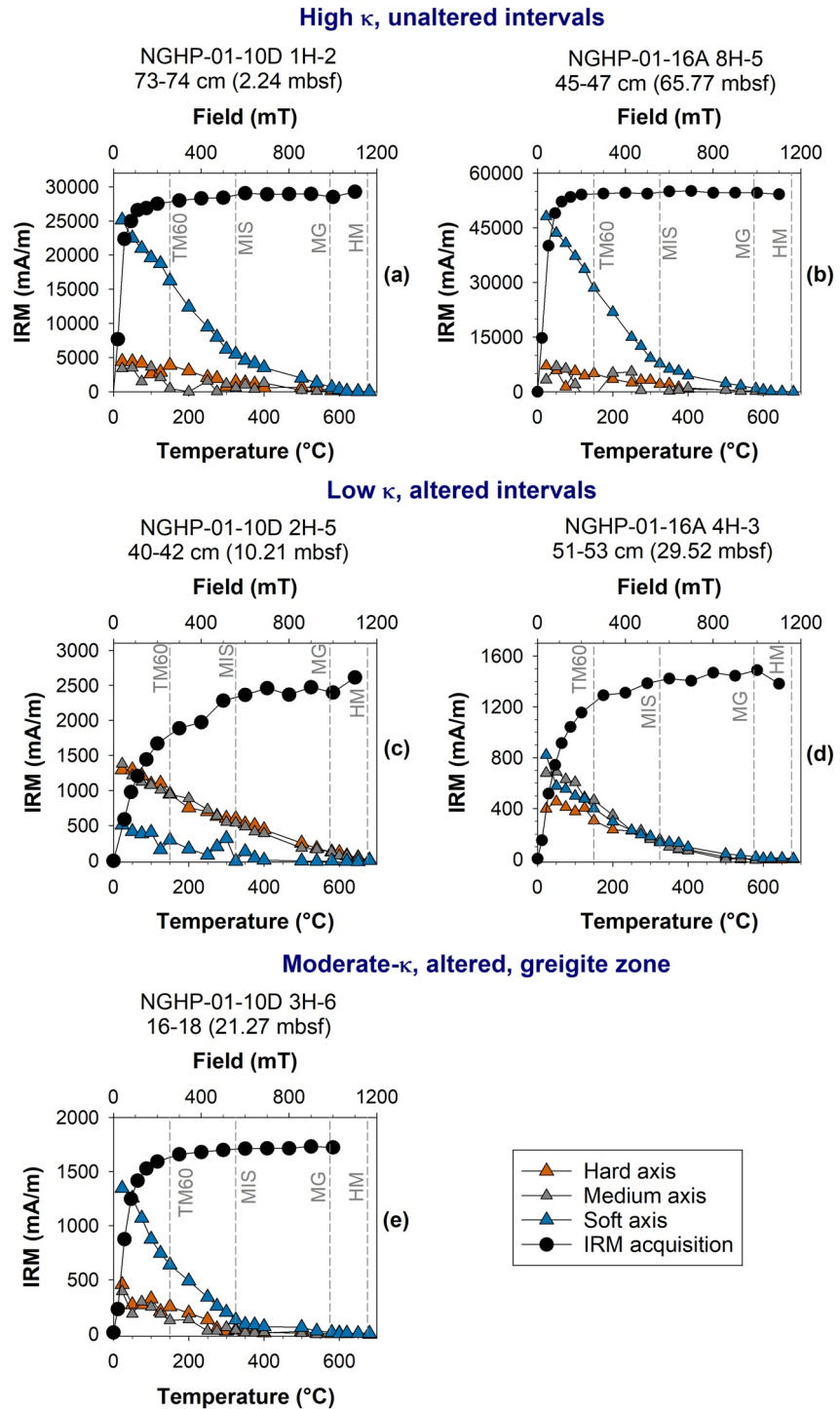
**Figure 4.** IRM acquisition and three-axis thermal demangetization curves for Sites 10 (a, c, e) and Site 16 (b and d). We show example curves for unaltered κ intervals (a and b), altered κ-pyritization (c and d), and altered κ-gregite-bearing (e) intervals. Vertical dashed lines represent the Curie temperatures for magnetite (MG), TM60 titanomagnetite, and hematite (HM) and the unblocking temperature for the magnetic iron sulfides (MIS) greigite and pyrrhotite.
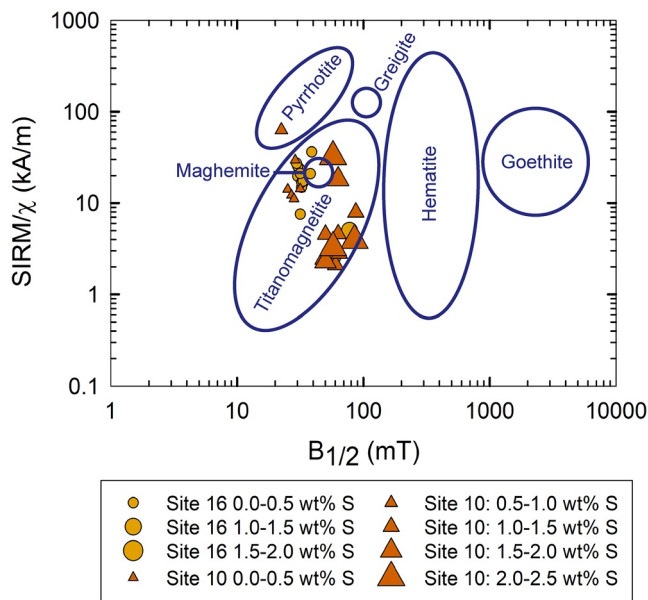
**Figure 5.** Cross plot of SIRM/$\chi$ and $B_{1/2}$ for Site 10 (circles) and Site 16 (triangles). Larger symbol sizes indicate higher total sulfur content. Magnetic mineral ranges are from Peters and Dekkers ([2003]).

titanomagnetite loss (wt%) can be used to calculate a predicted pyrite sulfur profile, which we then compare with TS measurements. This approach allows us to correlate intervals of decreased $\kappa$ (i.e., those decoupled from Zr/Rb) with an additional indicator of sulfide mineralization.

### 4.2. Titanomagnetite Loss and Pyrite Gain

In the presence of reactive Fe and $H_2S$, pyrite formation occurs in the anoxic zone in marine sediments. After the most reactive Fe (oxyhydr)oxide phases (hydrous ferric-oxides, lepidocrocite) are consumed, magnetite and then hematite become primary sources of reactive Fe for pyrite formation (Poulton et al., [2004]). Applying the approach described above to the records from Sites 16 and 10, we show that the predicted pyrite S and measured bulk TS profiles, both distinctly increase in the zones of depleted $\kappa$ (Figure [6]). While the observed TS is an order of magnitude higher than predicted pyrite S based on a TM60 composition, they show relative increases in S in the same intervals. Our predicted pyrite S content matches closest when based on the $\kappa$ of ülvospinel, which is not likely the dominant titanomagnetite composition based on a Deccan source more similar to TM60 (Radhakrishnamurty & Subbrao, [1990]). Uncertainty in the titanomagnetite composition, reaction of $H_2S$ with dissolved Fe and other Fe-(oxyhydr)oxides, and formation of iron monosulfides, elemental sulfur and organic sulfur compounds may contribute to the discrepancy in absolute wt% estimates between predicted and observed S. The most depleted zones of $\kappa$ (30–35 mbsf at Site 16 and 10–27 mbsf at Site 10) have TS > 1 wt%. A pyrite nodule was also observed at 35 mbsf at Site 16 (see Figure [S5]). The Fe/$\kappa$ profile reveals the zones of maximum $\kappa$ loss (increased paramagnetic rather than ferrimagnetic Fe), which are coincident with the TS gains and predicted pyrite S increases throughout both records (Figure [6]). The increases in Fe/$\kappa$ are consistent with higher pyrite and lower titanomagnetite content. Intervals with no depleted $\kappa$ (e.g., Site 16, 36–56 mbsf) show systematically less TS (0.15 wt% mean) than in the zones of reduced $\kappa$ (0.59 wt% mean) (Figure [6]). Collectively, these relationships indicate that the intervals of correlated maximum $\kappa$ loss and TS gain are diagenetically altered, where reaction of $H_2S$ with titanomagnetite produced reactive Fe that contributed to increased TS (pyrite formation), reducing $\kappa$.

## 5. Discussion

### 5.1. Tracking Paleo-SMTZ Positions

Based on the results presented above, we attribute the depleted $\kappa$ in the Site 16 and 10 records to pyritization fronts preserved in the sediments. The data suggest a scenario where the SMTZ remained fixed at a given paleo-depth for some period of time, followed by an upward migration of this horizon.

#### 5.1.1. Site 16

At Site 16, the modern SMTZ depth (23 mbsf) is 6–12 m shallower than the most pronounced decrease in $\kappa$ (29–35 mbsf) (Figure [6a]). This depth difference corresponds to eight meters of sediment that accumulated during the Holocene (Figure [6a]) (Ponton et al., [2012]). A rapid increase in monsoonal weathering and sediment accumulation following the slowdown in sedimentation on this margin during glacial periods, described by (Phillips, Johnson, Giosan, & Rose, [2014]), would rapidly drive a stalled SMTZ to shallower depths (e.g., Riedinger et al., [2005]). The slowdown in sedimentation rate during glacial periods would allow sufficient time for pyritization to draw down the $\kappa$ signal, whereas the increase in post-glacial sedimentation rate that drives a continuously upward migration of the SMTZ, allows less time for pyritization and consequently a smaller loss of $\kappa$ farther up the record.

The presence of methane-derived authigenic carbonates (MDAC) (e.g., Ritger et al., [1987]) can also indicate paleo-positions of the SMTZ. At Site 16, the only MDAC (low-Mg) calcite at 31.4 mbsf (Figure [S5]) is
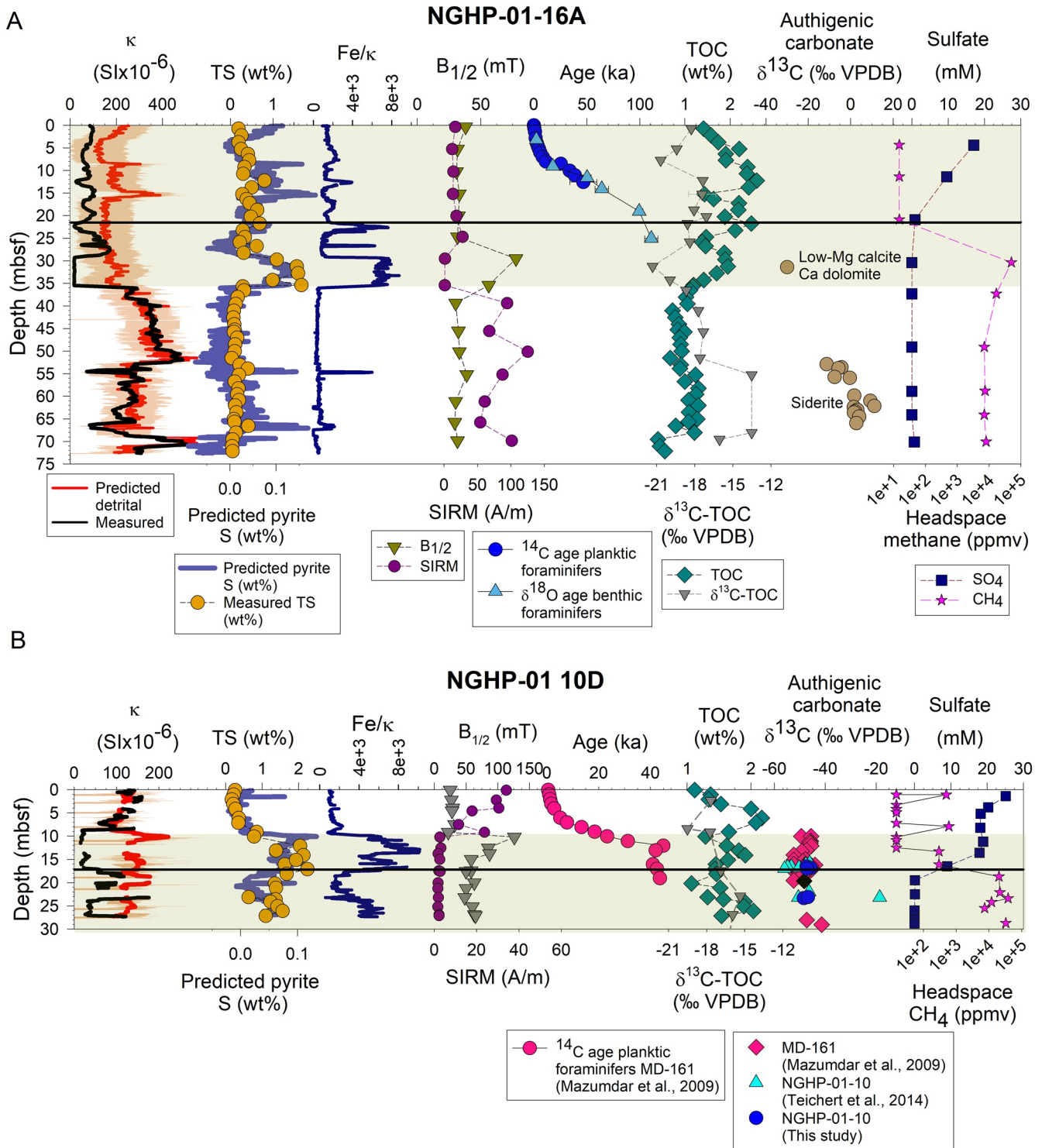
**Figure 6.** Summary plots for Site 16 (a) and Site 10 (b) showing the diagenetically altered zones of κ correspond to increased TS, consistent with titanomagnetite dissolution by $H_2S$ and precipitation of pyrite in $H_2S$ bearing sediments. Altered κ is also demonstrated as positive excursions in the Fe/κ. δ13C-depleted authigenic carbonates (Mg-calcite) in the altered κ zones suggests a significant role of AOM at these positions, while δ13C-enriched siderites below these intervals are indicative of methanogenesis coupled with silicate weathering (Solomon et al., 2014; Teichert et al., 2014; Torres et al., 2020). Porewater sulfate and headspace methane profiles define the modern SMTZ (horizontal black lines) at both sites. For reference seawater sulfate is ~28 mM. Age model from Site 10 from the companion MD-161 site (Mazumdar et al., 2009). Age model from Site 16 is a compilation of Ponton et al. (2012) and this study.

located within the most pronounced κ drawdown and is the most depleted δ^{13}C (−30 ‰ VPDB) carbonate in the examined core interval (Figure 6a), consistent with our reconstructions. Below this depth, and within predominantly unaltered κ, authigenic carbonates transition to more enriched δ^{13}C (−11 to +11 ‰ VPDB) values (Figure 6a) and Fe-rich carbonates (e.g., siderite between 52 and 66 mbsf; see Figure S3), which represent a separate pathway for carbonate formation not related to AOM. Rather, these enriched carbonates are associated with silicate weathering reactions coupled to microbial methanogenesis described by Solomon et al. (2014) and Torres et al. (2020), which do not affect κ.

Less clear are inferences based on the absence of authigenic carbonates above the largest drawdown in κ at Site 16, in sediments with an observed κ loss above the modern SMTZ. There is an approximate doubling of TOC in the upper 35 mbsf (1.87 wt% from 0.96 wt% below 35 mbsf) at Site 16. OSR rates often exceed the rates of AOM at non-seep sites (Hinrichs & Boetius, 2002), thus, the dramatic change in organic matter availability at Site 16 may have driven OSR to produce enough $H_2S$ to reduce κ. The lack of authigenic carbonates in the upper 35 mbsf may be explained by insufficient time to precipitate them from bicarbonate produced solely from OSR and/or authigenic carbonates are sufficiently small, present as micro-crystals (e.g., Rose et al., 2014), thus not observed during split core description or in smear slides from this stratigraphy (Collett et al., 2015). Nevertheless, the κ record at Site 16, appears to have been altered by both AOM and OSR, perhaps independently (see additional discussion in Section 5.2).

In contrast, in the deeper sediments below 35 mbsf, the unaltered κ retains its signal from primary detrital mineral inputs. Within this interval, nannofossil and foraminifera abundance remains low (Collett et al., 2015) and $CaCO_3$ is less than 12 wt% (Johnson et al., 2014). The lower TOC content below 35 mbsf has remarkably higher δ^{13}C-TOC (−18 to −13 ‰VPDB) (Johnson et al., 2014), consistent with higher fraction of vegetation from terrestrial sources that are extensive on the Indian subcontinent during the Plio-Pleistocene (Dunlea et al., 2020; Galy et al., 2008).The lack of diagenetic loss of κ in the lower part of the record could be explained by low OSR rates that correspond to the observed lower TOC abundance and/or a quickly migrating SMTZ driven by possible higher sedimentation rates.

### 5.1.2. Site 10

At Site 10, the diagenetic drawdown in κ (9–27 mbsf) corresponds to intervals with abundant MDAC (Figure 6b) (Mazumdar et al., 2009; Teichert et al., 2014) and [34]S-enriched chromium reducible sulfur (CRS) (Peketi et al., 2012) that suggest AOM at the modern and deeper paleo-SMTZs. The presence of paleo-seep fauna (Collett et al., 2015; Gale et al., 2020; Mazumdar et al., 2009) and Mo anomalies (Peketi et al., 2012) further indicate that paleo-methane seepage may have breached the seafloor at this site. AOM rates at methane seeps are 1–2 orders of magnitude higher than buried SMTZs where methane supply is dominated by diffusion (Knittel & Boetius, 2009). The paleo-seep conditions at Site 10 and associated high $H_2S$ production rates likely contributed to the very high TS content (as high as 2.2 wt%) measured in this interval. The apparent diagenetic decrease in κ at Site 10 is limited however, between 17 and 23 mbsf, due to the presence of greigite or sufficient ferrimagnetic iron oxides that maintain moderate values of κ that are not much less than the detrital background.

### 5.2. TS Versus TOC

To investigate whether pyritization is linked to the supply of organic matter, we compare the measured TS to TOC, and deviations from expected trends, to the κ record. The records from Site 10 and Site 16 (between 29 and 35 mbsf) have intervals of reduced κ that correspond to higher TS than expected if pyritization was driven only by OSR (Figure 7; Berner & Raiswell, 1983). These high TS intervals may be a first order indicator of AOM-driven pyritization (e.g., Kaneko et al., 2010) and prolonged paleo-positions of the SMTZ. In the reduced κ sediments above 29 mbsf at Site, the TS to TOC ratio is consistent with that predicted from OSR, rather than AOM (Figure 7a). In general, the lowest values of κ (<50 SI x 10^{−6}) correspond to high TS/TOC associated with AOM while reduced κ values (50–200 SI x 10^{−6}) correspond to TOC values >1.5 wt% associated with enhanced OSR (Figure 7b). Our data show paleo-preservation of the diagenetic κ loss, which at Site 10 are similar to values observed at modern seeps with sustained high methane fluxes (Novosel et al., 2005), and at Site 16 match those reported at modern stalled SMTZs (Riedinger et al., 2005). It is notable that the mobility of methane, which can be generated *in situ* or supplied from deeper sediments,
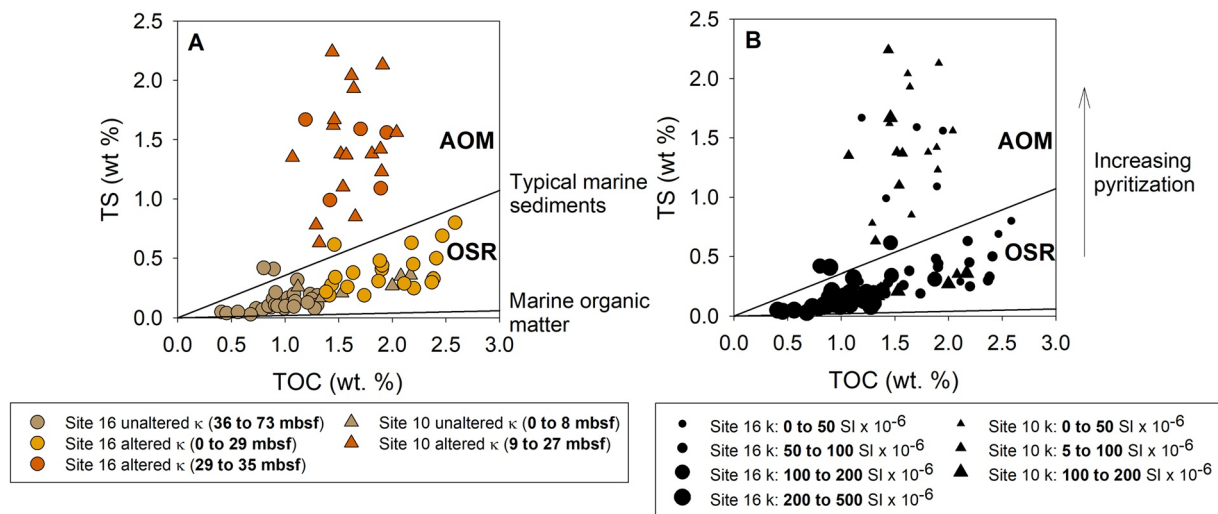
**Figure 7.** TS versus TOC cross plot to document excess sulfur (above normal marine sediment line) present in the diagenetically altered zones at Sites 16 and 10, which is consistent with AOM (Kaneko et al., 2010). Normal marine sediment line of 3:1 TOC:TS due to OSR from Berner and Raiswell (1983). Marine organic matter line 50:1 TOC:TS from Suits and Arthur (2000). (a) Red triangles represent the interval of altered κ between 9 and 27 mbsf at Site 10. Red circles represent the interval of altered κ between 29 and 35 mbsf at Site 16. Orange circles represent the interval of altered κ between 0 and 29 mbsf at Site 16. Brown triangles and circles represent intervals of unaltered κ from Site 10 (0–8 mbsf) and Site 16 (36–73 mbsf). (b) The size of the circles (Site 16) or triangles (Site 10) increase with higher values of κ.

relative to TOC, may help enhance AOM-driven pyritization. OSR-driven pyritization and dissimilatory iron reduction (Hepp et al., 2009; Passier et al., 2001) on the other hand, which can impact κ, may be limited by the *in situ* type and fixed amount of TOC in the sediments. Together, both Sites 10 and 16 demonstrate the potential of our approach to identify intervals of past pyritization of titanomagnetite, which may be driven by changes in sedimentation rate, TOC availability, and/or episodic methane fluxes.

### 5.3. Fe-Oxides, Pyritization, and Chemosynthetic Biological Communities

The role of Fe-oxide minerals as a source of iron for pyritization is important in this and in many continental margin environments, where high rates of sedimentation efficiently bury labile organic carbon below the oxic zone to fuel sulfate reduction (Berner, 1978). Full pyritization occurs when the rate of sulfide production exceeds that of reactive iron burial (Roberts, 2015). AOM generates sulfide in excess of that generated by OSR, which, in addition to iron burial, regulates the sulfide availability. Chemosynthetic biological communities (CBCs) at methane seeps rely on $H_2S$ to sustain their symbionts (Dale et al., 2010). In marine sediments with high Fe-oxide content, consumption of $H_2S$ during pyritization can result in the absence of dissolved $H_2S$ even during ongoing sulfate reduction (Canfield, 1989). When iron oxides are depleted through organic metabolic pathways in the Fe reduction zone and/or reaction with $H_2S$ (as indicated here by decreased κ) and subsequent pyritization (as mapped here by TS), excess $H_2S$ will become available for utilization by CBCs. Since the presence of iron oxides in the sediments efficiently controls the amount of sulfide sequestration as pyrite (Canfield, 1989), seafloor chemosynthetic activity is viable when the supply and reactivity of the iron oxides is low enough for the rate of sulfide production to exceed the rate of iron sulfide formation.

At Site 10, a full κ drawdown at 16 mbsf is preserved in concert with a fossilized paleo-seep community. Here, reactive iron was exhausted, allowing bioavailable $H_2S$ to reach the seafloor at a high enough rate to initiate and sustain CBC development. Gravity cores from the Krishna-Godavari basin show decreased κ in cores with SMTZs at 4–5 msbf (Usapkar et al., 2014), indicating that in systems where the SMTZ is shallow, $H_2S$ produced via AOM at the SMTZ results in the dissolution of Fe-oxides in close proximity to the seafloor. At Site 10 and other methane seep environments, variable fluxes of $H_2S$ produced by AOM can effectively mine the Fe released from Fe-oxides out of the sediments to precipitate Fe-sulfides. The detrital Fe-oxide distribution in marine sediments can therefore play a major role in regulating maximum pyritization at

methane seeps, as shown here for Site 10 and in agreement with observations elsewhere. The global sulfur sink in marine sediments has been attributed to pyrite sulfur sequestration (Berner & Raiswell, 1983). Here we argue that at methane seeps the $H_2S$ generated by AOM can fully deplete available detrital sources of Fe needed to precipitate Fe sulfide minerals, limiting the capacity of marine sediments to sequester sulfur globally, yet potentially sustaining seafloor CBC's. In contrast, methane seeps on continental margins with abundant detrital magnetic minerals, may help sustain marine sediment pyritization, enhancing the marine sediment sulfur sink, yet potentially limiting the development of CBC's.

### 5.4. Applicability of This Approach

Our approach for isolating detrital and diagenetic signals in magnetic susceptibility records of methane-bearing marine sediments requires the following conditions: (a) the presence and persistence of detrital Fe-oxides (magnetite or hematite), zircon, and other Ti-bearing heavy minerals (e.g., titanomagnetite, ilmenite, or rutile) that can be detected using XRF core scanning technology; (b) no significant presence of diagenetic magnetic Fe-sulfides (greigite or pyrrhotite) that can locally increase κ; (c) reference sections or sites where κ is not diagenetically altered; and (d) sufficient sub-seafloor TOC preservation to drive OSR and methanogenesis. In general, this approach is suitable for continental margins with a substantial lithogenic input and a terrigenous and/or marine organic carbon flux that is high enough to drive OSR and methanogenesis. Magnetite-dominant lithogenic sources provide an ideal setting because the κ of magnetite is >25 times higher than hematite or goethite (Hunt et al., 1995). Mixed assemblages of magnetite with higher abundance of other iron oxide phases may introduce additional errors since the reaction of these iron oxides with $H_2S$ generates a larger sulfur sink than that predicted by κ loss. In addition to Zr/Rb, Ti associated with titanomagnetite, ilmenite, and rutile can provide an alternative means of tracking heavy minerals using the Ti/Rb or Ti/K ratio (Figure S6).

### 6. Conclusions

Integration of κ with Zr/Rb (from XRF) records in titanomagnetite-bearing marine sediments can be used to identify intervals of diagenetic loss of κ. Using data from the Krishna-Godavari Basin (NGHP-01 Sites 10 and 16) we demonstrate that predicted pyrite sulfur, based on the assumption of full pyritization of titanomagnetite, correlates to the pattern of measured total sulfur, except where greigite is present. By integrating this analysis with additional sedimentological and diagenetic proxies, we can associate observed diagenetic drawdowns in κ with paleo-SMTZ positions, intervals of increased TOC deposition, and methane venting. Additionally, plots of TOC versus TS can help distinguish alteration of κ and pyrite precipitation driven by OSR or AOM. This approach is applicable on continental margins with a consistent input of detrital Fe-oxides and zircon, and sufficient TOC to drive OSR and methanogenesis. Sediments in titanomagnetite-dominated margins are efficient sediment sinks for global sulfur as sedimentary pyrite, produced from $H_2S$ generated via OSR and AOM. This pyritization process may limit the $H_2S$ available to chemosynthetic seep fauna until *in situ* detrital sources of Fe are fully depleted. Under conditions of reactive iron depletion, such as those in methane cold seeps, the pyrite-sulfur sink ceases to operate, and sulfide escapes the sediment to be consumed by chemosynthesis or abiotic oxidation reactions.

### Data Availability Statement

The data presented in this paper are accessible through the PANGEA database (https://doi.pangaea.de/10.1594/PANGAEA.933230).

### References

Anitha, G., Ramana, M. V., Ramprasad, T., Dewangan, P., & Anuradha, M. (2014). Shallow geological environment of Krishna–Godavari offshore, eastern continental margin of India as inferred from the interpretation of high resolution sparker data. *Journal of Earth System Science*, *123*, 329–342. https://doi.org/10.1007/s12040-013-0399-3

Badesab, F., Dewangan, P., Gaikwad, V., Kars, M., Kocherla, M., Krishna, K. S., et al. (2019). Magnetic mineralogical approach for the exploration of gas hydrates in the Bay of Bengal. *Journal of Geophysical Research: Solid Earth*, *124*, 4428–4451. https://doi.org/10.1029/2019JB017466

Badesab, F., Dewangan, P., Gaikwad, V., Sebastian, J. G., & Venkateshwarlu, M. (2020). A rock magnetic perspective of gas hydrate occurrences in a high-energy depositional system in the Krishna-Godavari basin, Bay of Bengal. *Geo-Marine Letters*, *40*, 525–539. https://doi.org/10.1007/s00367-020-00646-8

Badesab, F., Dewangan, P., Usapkar, A., Kocherla, M., Peketi, A., Mohite, K., et al. (2017). Controls on evolution of gas-hydrate system in the Krishna-Godavari basin, offshore India. *Geochemistry, Geophysics, Geosystems*, *18*, 52–74. https://doi.org/10.1002/2016gc006606

Badesab, F., Gaikwad, V., Nath, B. N., Venkateshwarlu, M., Aiswarya, P. V., Tyagi, A., et al. (2021). Controls of contrasting provenance and fractionation on the sediment magnetic records from the Bay of Bengal. *Marine Geology*, *437*, 106515. https://doi.org/10.1016/j.margeo.2021.106515

Banerjee, R., & Mondal, S. K. (2021). Petrology and geochemistry of the Deccan basalts from the KBH-7 borehole, Koyna Seismic Zone (Western Ghats, India): Implications for nature of crustal contamination and sulfide saturation of magma. *Lithos*, *380–381*, 380–381. https://doi.org/10.1016/j.lithos.2020.105864

Barnes, R. O., & Goldberg, E. D. (1976). Methane production and consumption in marine sediments. *Geology*, *4*, 297–300. https://doi.org/10.1130/0091-7613(1976)4<297:MPACIA>2.0.CO;2

Berner, R. A. (1970). Sedimentary pyrite formation. *American Journal of Science*, *268*, 1–23. https://doi.org/10.2475/ajs.268.1.1

Berner, R. A. (1978). Sulfate reduction and the rate of deposition in marine sediments. *Earth and Planetary Science Letters*, *37*, 492–498. https://doi.org/10.1016/0012-821X(78)90065-1

Berner, R. A. (1984). Sedimentary pyrite formation: An update. *Geochimica et Cosmochimica Acta*, *48*, 605–615. https://doi.org/10.1016/0016-7037(84)90089-9

Berner, R. A., & Raiswell, R. (1983). Burial of organic carbon and pyrite sulfur in sediments over Phanerozoic time: A new theory. *Geochimica et Cosmochimica Acta*, *47*, 855–862. https://doi.org/10.1016/0016-7037(83)90151-5

Biksham, G., & Subramanian, V. (1988). Sediment transport of the Godavari River basin and its controlling factors. *Journal of Hydrology*, *101*, 275–290. https://doi.org/10.1016/0022-1694(88)90040-6

Boetius, A., Ravenschlag, K., Schubert, C. J., Rickert, D., Widdel, F., Gieseke, A., et al. (2000). A marine microbial consortium apparently mediating anaerobic oxidation of methane. *Nature*, *407*, 623–626. https://doi.org/10.1038/35036572

Bose, M. K. (1972). Deccan basalts. *Lithos*, *5*, 131–145. https://doi.org/10.1016/0024-4937(72)90065-5

Boswell, R., Yoneda, J., & Waite, W. F. (2019). India National Gas Hydrate Program Expedition 02 summary of scientific results: Evaluation of natural gas-hydrate-bearing pressure cores. *Marine and Petroleum Geology*, *108*, 143–153. https://doi.org/10.1016/j.marpetgeo.2018.10.020

Canfield, D. E. (1989). Reactive iron in marine sediments. *Geochimica et Cosmochimica Acta*, *53*, 619–632. https://doi.org/10.1016/0016-7037(89)90005-7

Canfield, D. E., & Berner, R. A. (1987). Dissolution and pyritization of magnetite in anoxic marine sediments. *Geochimica et Cosmochimica Acta*, *51*, 645–659. https://doi.org/10.1016/0016-7037(87)90076-7

Chang, L., Bolton, C. T., Dekkers, M. J., Hayashida, A., Heslop, D., Krijgsman, W., et al. (2016). Asian monsoon modulation of nonsteady state diagenesis in hemipelagic marine sediments offshore of Japan. *Geochemistry, Geophysics, Geosystems*, *17*, 4383–4398. https://doi.org/10.1002/2016GC006344

Chen, J., Chen, Y., Liu, L., Ji, J., Balsam, W., Sun, Y., & Lu, H. (2006). Zr/Rb ratio in the Chinese loess sequences and its implication for changes in the East Asian winter monsoon strength. *Geochimica et Cosmochimica Acta*, *70*, 1471–1482. https://doi.org/10.1016/j.gca.2005.11.029

Choudhuri, M., Guha, D., Dutta, A., Sinha, S., & Sinha, N. (2010). Spatiotemporal variations and kinematics of shale mobility in the Krishna-Godavari basin, India. In Wood, L. (Ed.), *Shale tectonics: AAPG Memoir 93* (pp. 91–109). https://doi.org/10.1306/13231310M933420

Clemens, S. C., Yamamoto, M., Thirumalai, K., Giosan, L., Richey, J. N., Nilsson-Kerr, K., et al. (2021). Remote and local drivers of Pleistocene South Asian summer monsoon precipitation: A test for future predictions. *Science Advances*, *7*, eabg3848. https://doi.org/10.1126/sciadv.abg3848

Colin, C., Kissel, C., Blamart, D., & Turpin, L. (1998). Magnetic properties of sediments in the Bay of Bengal and the Andaman Sea: Impact of rapid North Atlantic Ocean climatic events on the strength of the Indian monsoon. *Earth and Planetary Science Letters*, *160*, 623–635. https://doi.org/10.1016/S0012-821X(98)00116-2

Collett, T., Riedel, M., Cochran, J., Boswell, R., Presley, J., Kumar, P., et al. (2015). Indian National Gas Hydrate Program Expedition 01 report. In *U.S. Geological Survey Scientific Investigations Report 2012–5054*. (p. 1442). https://doi.org/10.3133/sir20125054

Collett, T. S., Boswell, R., Waite, W. F., Kumar, P., Roy, S. P., Chopra, K., et al. (2019). India National Gas Hydrate Program Expedition 02 Summary of Scientific Results: Gas hydrate systems along the eastern continental margin of India. *Marine and Petroleum Geology*, *108*, 39–142. https://doi.org/10.1016/j.marpetgeo.2019.05.023

Cook, A. E., Goldberg, D. S., & Malinverno, A. (2014). Natural gas hydrates occupying fractures: A focus on non-vent sites on the Indian continental margin and the northern Gulf of Mexico. *Marine and Petroleum Geology*, *58A*, 278–291. https://doi.org/10.1016/j.marpetgeo.2014.04.013

Dale, A. W., Sommer, S., Haeckel, M., Wallmann, K., Linke, P., Wegener, G., & Pfannkuche, O. (2010). Pathways and regulation of carbon, sulfur and energy transfer in marine sediments overlying methane gas hydrates on the Opouawe Bank (New Zealand). *Geochimica et Cosmochimica Acta*, *74*, 5763–5784. https://doi.org/10.1016/j.gca.2010.06.038

Dewangan, P., Basavaiah, N., Badesab, F. K., Usapkar, A., Mazumdar, A., Joshi, R., & Ramprasad, T. (2013). Diagenesis of magnetic minerals in a gas hydrate/cold seep environment off the Krishna–Godavari basin, Bay of Bengal. *Marine Geology*, *340*, 57–70. https://doi.org/10.1016/j.margeo.2013.04.016

Dewangan, P., Ramprasad, T., Ramana, M. V., Mazumdar, A., Desa, M., & Badesab, F. K. (2010). Seabed morphology and gas venting features in the continental slope region of Krishna–Godavari basin, Bay of Bengal: Implications in gas-hydrate exploration. *Marine and Petroleum Geology*, *27*, 1628–1641. https://doi.org/10.1016/j.marpetgeo.2010.03.015

Dixit, G., Ram, H., & Kumar, P. (2019). Origin of gas in gas hydrates as interpreted from geochemistry data obtained during the National Gas Hydrate Program Expedition 02, Krishna Godavari Basin, offshore India. *Marine and Petroleum Geology*, *108*, 389–396. https://doi.org/10.1016/j.marpetgeo.2018.11.047

Dunlea, A. G., Giosan, L., & Huang, Y. (2020). Pliocene expansion of C4 vegetation in the Core Monsoon Zone on the Indian Peninsula. *Climate of the Past*, *16*, 2533–2546. https://doi.org/10.5194/cp-16-2533-2020

Dutta, K., Bhushan, R., & Somayajulu, B. L. K. (2001). ΔR correction values for the Northern Indian Ocean. *Radiocarbon*, *43*, 483–488. https://doi.org/10.1017/S0033822200038376

Dypvik, H., & Harris, N. B. (2001). Geochemical facies analysis of fine-grained siliciclastics using Th/U, Zr/Rb and (Zr + Rb)/Sr ratios. *Chemical Geology*, *181*, 131–146. https://doi.org/10.1016/S0009-2541(01)00278-9

Flores, J. A., Johnson, J. E., Mejía-Molina, A. E., Álvarez, M. C., Sierro, F. J., Singh, S. D., et al. (2014). Sedimentation rates from calcareous nannofossil and planktonic foraminifera biostratigraphy in the Andaman Sea, northern Bay of Bengal, and eastern Arabian Sea. *Marine and Petroleum Geology*, *58*, 425–437. https://doi.org/10.1016/j.marpetgeo.2014.08.011

Gaikwad, V., Badesab, F., Dewangan, P., & Kotha, M. (2021). Diagenesis of magnetic minerals in active/relict methane seep: Constraints from rock magnetism and mineralogical records from Bay of Bengal. *Frontiers of Earth Science*, *9*, 638594. https://doi.org/10.3389/feart.2021.638594

Gale, A. S., Little, C. T. S., Johnson, J. E., & Giosan, L. (2020). A new neolepadid cirripede from a Pleistocene cold seep, Krishna-Godavari Basin, offshore India. *Acta Palaeontologica Polonica*, *65*(2), 351–362. https://doi.org/10.4202/app.00705.2019

Galy, V., Francois, L., France-Lanord, C., Faure, P., Kudrass, H., Palhol, F., & Singh, S. K. (2008). C4 plants decline in the Himalayan basin since the Last Glacial Maximum. *Quaternary Science Reviews*, *27*, 1396–1409. https://doi.org/10.1016/j.quascirev.2008.04.005

Garming, J. F. L., Bleil, U., & Riedinger, N. (2005). Alteration of magnetic mineralogy at the sulfate-methane transition: Analysis of sediments from the Argentine continental slope. *Physics of the Earth and Planetary Interiors*, *151*, 290–308. https://doi.org/10.1016/j.pepi.2005.04.001

Gebregiorgis, D., Giosan, L., Hathorne, E. C., Anand, P., Nilsson-Kerr, K., Plass, A., et al. (2020). What can we learn from X-ray fluorescence core scanning data? A paleomonsoon case study. *Geochemistry, Geophysics, Geosystems*, *21*, e2019GC008414. https://doi.org/10.1029/2019GC008414

Giosan, L., Ponton, C., Usman, M., Blusztajn, J., Fuller, D. Q., Galy, V., et al. (2017). Massive erosion in monsoonal central India linked to late Holocene land cover degradation. *Earth Surface Dynamics*, *5*, 781–789. https://doi.org/10.5194/esurf-5-781-2017

Hatfield, R. G., Stoner, J. S., Reilly, B. T., Tepley, F. J., Wheeler, B. H., & Housen, B. A. (2017). Grain size dependent magnetic discrimination of Iceland and South Greenland terrestrial sediments in the northern North Atlantic sediment record. *Earth and Planetary Science Letters*, *474*, 474–489. https://doi.org/10.1016/j.epsl.2017.06.042

Hatfield, R. G., Wheeler, B. H., Reilly, B. T., Stoner, J. S., & Housen, B. A. (2019). Particle size specific magnetic properties across the Norwegian-Greenland Seas: Insights into the influence of sediment source and texture on bulk magnetic records. *Geochemistry, Geophysics, Geosystems*, *20*, 1004–1025. https://doi.org/10.1029/2018GC007894

Heaton, T. J., Köhler, P., Butzin, M., Bard, E., Reimer, R. W., Austin, W. E. N (2020). Marine20—The Marine Radiocarbon Age Calibration Curve (0–55,000 cal BP). *Radiocarbon*, *62*(4), 779–820. https://doi.org/10.1017/RDC.2020.68

Hepp, D. A., Mörz, T., Hensen, C., Frederichs, T., Kasten, S., Riedinger, N., & Hay, W. F. (2009). A late Miocene-early Pliocene Antarctic deepwater record of repeated iron reduction events. *Marine Geology*, *266*, 198–211. https://doi.org/10.1016/j.margeo.2009.08.006

Hinrichs, K.-U., & Boetius, A. (2002). The anaerobic oxidation of methane: New insights in microbial ecology and biogeochemistry. In Wefer, G., et al. (Eds.), *Ocean margin systems* (pp. 457–477). Berlin: Springer-Verlag. https://doi.org/10.1007/978-3-662-05127-6_28

Hinrichs, K.-U., Hayes, J. M., Sylva, S. P., Brewer, P. G., & Delong, E. F. (1999). Methane-consuming archeabacteria in marine sediments. *Nature*, *398*, 802–805. https://doi.org/10.1038/19751

Holland, M. E., & Schultheiss (2014). Comparison of methane mass balance and X-ray computed tomographic methods for calculation of gas hydrate content of pressure cores. *Marine and Petroleum Geology*, *58*, 168–177. https://doi.org/10.1016/j.marpetgeo.2014.07.016

Hong, W.-L., Solomon, E. A., & Torres, M. E. (2014). A kinetic-model approach to quantify the effect of mass transport deposits on pore water profiles in the Krishna-Godavari Basin, Bay of Bengal. *Marine and Petroleum Geology*, *58A*, 223–232. https://doi.org/10.1016/j.marpetgeo.2014.06.014

Housen, B. A., & Musgrave, R. J. (1996). Rock-magnetic signature of gas hydrates in accretionary prism sediments. *Earth and Planetary Science Letters*, *139*, 509–519. https://doi.org/10.1016/0012-821X(95)00245-8

Hunt, C. P., Moskowitz, B. M., & Banerjee, S. K. (1995). Magnetic properties of rocks and minerals. In Ahrens, T. J. (Ed.), *Rock physics & phase relations: A handbook of physical constants* (pp. 189–204). Washington, D. C.: American Geophysical Union. https://doi.org/10.1029/RF003p0189

Imbrie, J., Hays, J. D., Martinson, D. G., McIntyre, Mix, A. C., Morely, J. J., et al. (1984). The orbital theory of Pleistocene climate: Support from a revised chronology of the marine $\delta^{18}O$ record. In Berger, A. L., et al. (Eds.), *Milankovitch and climate part I* (pp. 269–305).

Jaiswal, P., Al-Bulushi, S., & Dewangan, P. (2014). Logging-while-drilling and wireline velocities: Site NGHP-01-10, Krishna–Godavari Basin, India. *Marine and Petroleum Geology*, *58A*, 331–338. https://doi.org/10.1016/j.marpetgeo.2014.05.006

Jaiswal, P., Dewangan, P., Ramprasad, T., & Zelt, C. A. (2012). Seismic characterization of hydrates in faulted, fine-grained sediments of Krishna-Godavari Basin: Full waveform inversion. *Journal of Geophysical Research*, *112*. https://doi.org/10.1029/2012JB009201

João, H. M., Badesab, F., Gaikwad, V., Kocherla, M., & Deenadayalan, K. (2021). Controls of mass transport deposit and magnetic mineral diagenesis on the sediment magnetic record from the Bay of Bengal. *Marine and Petroleum Geology*, *128*, 104994. https://doi.org/10.1016/j.marpetgeo.2021.104994

Johnson, G. R., & Olhoeft, G. R. (1984). Density of rocks and minerals. In Carmichael, R. S. (Ed.), *Handbook of physical properties of rocks* (Vol. 3, pp. 1–38). Boca Raton, FL: CRC Press.

Johnson, J. E., Phillips, S. C., Torres, M. E., Piñero, E., Rose, K. K., & Giosan, L. (2014). Influence of total organic carbon deposition on the inventory of gas hydrate in the Indian continental margins. *Marine and Petroleum Geology*, *58A*, 406–424. https://doi.org/10.1016/j.marpetgeo.2014.08.021

Joshi, R. K., Mazumdar, A., Peketi, A., Ramamurty, P. B., Naik, B. G., Kocherla, M., et al. (2014). Gas hydrate destabilization and methane release events in the Krishna–Godavari Basin, Bay of Bengal. *Marine and Petroleum Geology*, *58*, 476–489. https://doi.org/10.1016/j.marpetgeo.2014.08.013

Kale, V. S. (2007). Fluvio–sedimentary response of the monsoon-fed Indian rivers to Late Pleistocene–Holocene changes in monsoon strength: Reconstruction based on existing $^{14}C$ dates. *Quaternary Science Reviews*, *26*, 1610–1620. https://doi.org/10.1016/j.quascirev.2007.03.012

Kaneko, M., Shingai, H., Pohlman, J. W., & Naraoka, H. (2010). Chemical and isotopic signature of bulk organic matter and hydrocarbon biomarkers within mid-slope accretionary sediments of the northern Cascadia margin gas hydrate system. *Marine Geology*, *275*, 166–177. https://doi.org/10.1016/j.margeo.2010.05.010

Karlin, R., & Levi, S. (1983). Diagenesis of magnetic minerals in recent haemipelagic sediments. *Nature*, *303*, 327–330. https://doi.org/10.1038/303327a0

Kars, M., & Kodama, M. (2015). Authigenesis of magnetic minerals in gas hydrate-bearing sediments in the Nankai Trough, offshore Japan. *Geochemistry, Geophysics, Geosystems*, *16*, 947–961. https://doi.org/10.1002/2014GC005614

Kars, M., Musgrave, R. J., Kodama, K., Jonas, A.-S., Bordiga, M., Ruebsam, W., et al. (2017). Impact of climate change on the magnetic mineral assemblage in marine sediments from Izu rear arc, NW Pacific Ocean, over the last 1 Myr. *Palaeogeography, Palaeoclimatology, Palaeoecology*, *480*, 53–69. https://doi.org/10.1016/j.palaeo.2017.05.016

Kasten, S., Freudenthal, T., Gingele, F. X., & Schulz, H. D. (1998). Simultaneous formation of iron-rich layers at different redox boundaries in sediments of the Amazon deep-sea fan. *Geochimica et Cosmochimica Acta*, *62*, 2253–2264. https://doi.org/10.1016/S0016-7037(98)00093-3

Knittel, K., & Boetius, A. (2009). Anaerobic oxidation of methane: Progress with an unknown process. *Annual Review of Microbiology*, *63*, 311–334. https://doi.org/10.1146/annurev.micro.61.080706.093130

Kruiver, P. P., Dekkers, M. J., & Heslop, D. (2001). Quantification of magnetic coercivity components by the analysis of acquisition curves of isothermal remanent magnetization. *Earth and Planetary Science Letters*, *189*, 269–276. https://doi.org/10.1016/S0012-821X(01)00367-3

Kulkarni, Y. R., Sangode, S. J., Bloemendal, J., Meshram, D. C., & Suresh, N. (2015). Mineral magnetic characterization of the Godavari River and western Bay of Bengal sediments: Implications to source to sink relations. *Journal of the Geological Society of India*, *85*, 71–78. https://doi.org/10.1007/s12594-015-0194-7

Kulkarni, Y. R., Sangode, S. J., Meshram, D. C., Patil, S. K., & Dutt, Y. (2014). Mineral magnetic characterization of the Godavari River sediments: Implications to Deccan Basalt weathering. *Journal of the Geological Society of India*, *83*, 376–384. https://doi.org/10.1007/s12594-014-0054-x

Larrasoaña, J. C., Roberts, A. P., Musgrave, R. J., Gràcia, E., Piñero, E., Vega, M., & Martínez-Ruiz, F. (2007). Diagenetic formation of greigite and pyrrhotite in gas hydrate marine sedimentary systems. *Earth and Planetary Science Letters*, *261*, 350–366. https://doi.org/10.1016/j.epsl.2007.06.032

Lin, Q., Wang, J., Algeo, T. J., Sun, F., & Lin, R. (2016). Enhanced framboidal pyrite formation related to anaerobic oxidation of methane in the sulfate-methane transition zone of the northern South China Sea. *Marine Geology*, *379*, 100–108. https://doi.org/10.1016/j.margeo.2016.05.016

Lisiecki, L. E., & Raymo, M. E. (2005). A Pliocene-Pleistocene stack of 57 globally distributed benthic $\delta^{18}O$ records, *Paleoceanography*, *20*, PA1003, https://doi.org/10.1029/2004PA001071

Liu, Q., Roberts, A. P., Larrasoaña, J. C., Banerjee, S. K., Guyodo, Y., Tauxe, L., & Oldfield, F. (2012). Environmental magnetism: Principles and applications. *Reviews of Geophysics*, *50*, RG4002. https://doi.org/10.1029/2012RG000393

Lorenson, T. D., & Collett, T. S. (2018). National Gas Hydrate Program Expedition 01 offshore India; gas hydrate systems as revealed by hydrocarbon gas geochemistry. *Marine and Petroleum Geology*, *92*, 477–492. https://doi.org/10.1016/j.marpetgeo.2017.11.011

Lowrie, W. (1990). Identification of ferromagnetic minerals in a rock by coercivity and unblocking temperature properties. *Geophysical Research Letters*, *17*, 159–162. https://doi.org/10.1029/gl017i002p00159

Mandal, R., Dewangan, P., Ramprasad, T., Kumar, B. J. P., & Vishwanath, K. (2014). Effect of thermal non-equilibrium, seafloor topography and fluid advection on BSR-derived geothermal gradient. *Marine and Petroleum Geology*, *58A*, 368–381. https://doi.org/10.1016/j.marpetgeo.2014.04.002

März, C., Hoffman, J., Bleil, U., de Lange, G. J., & Kasten, S. (2008). Diagenetic changes of magnetic and geochemical signals by anaerobic methane oxidation in sediments of the Zambezi deep-sea fan (SW Indian Ocean). *Marine Geology*, *255*, 118–130. https://doi.org/10.1016/j.margeo.2008.05.013

Maxbauer, D. P., Feinberg, D. M., & Fox, D. L. (2016). Magnetic mineral assemblages in soils and paleosols as the basis for paleoprecipitation proxies: A review of magnetic methods and challenges. *Earth-Science Reviews*, *155*, 28–48. https://doi.org/10.1016/j.earscirev.2016.01.014

Mazumdar, A., Dewangan, P., Joäo, H. M., Peketi, A., Khosla, V. R., Kocherla, M., et al. (2009). Evidence of paleo-cold seep activity from the Bay of Bengal, offshore India. *Geochemistry, Geophysics, Geosystems*, *10*. https://doi.org/10.1029/2008GC002337

Mazumdar, A., Dewangan, P., Peketi, A., Gullapalli, S., Kalpana, M. S., Naik, G. P., et al. (2019). The first record of active methane (cold) seep ecosystem associated with shallow methane hydrate from the Indian EEZ. *Journal of Earth Systems Science*, *128*, 18. https://doi.org/10.1007/s12040-018-1044-y

Mazumdar, A., João, H. M., Peketi, A., Dewangan, P., Kocherla, M., Joshi, R. K., & Ramprasad, T. (2012). Geochemical and geological constraints on the composition of marine sediment pore fluid: Possible link to gas hydrate deposits. *Marine and Petroleum Geology*, *38*, 35–52. https://doi.org/10.1016/j.marpetgeo.2012.07.004

Mazumdar, A., Kocherla, M., Carvalho, M. A., Peketi, A., Joshi, R. K., Mahalaxmi, P., et al. (2015). Geochemical characterization of the Krishna-Godavari and Mahanadi offshore basin (Bay of Bengal) sediments: A comparative study of provenance. *Marine and Petroleum Geology*, *60*, 18–33. https://doi.org/10.1016/j.marpetgeo.2014.09.005

Mazumder, R., & Eriksson, P. G. (2015). Precambrian basins of India: Stratigraphic and tectonic context. In *Geological Society, London, Memoirs*. (Vol. 43, p. 352). https://doi.org/10.1144/M43.1

Milliman, J. D., & Meade, R. H. (1983). World-wide delivery of river sediment to the oceans. *Journal of Geology*, *36*, 1–21. https://doi.org/10.1086/628741

Musgrave, R. J., & Kars, M. (2016). Recognizing magnetostratigraphy in overprinted and altered marine sediments: Challenges and solutions from IODP Site U1437. *Geochemistry, Geophysics, Geosystems*, *17*, 3190–3206. https://doi.org/10.1002/2016GC006386

Novosel, I., Spence, G. D., & Hyndman, R. D. (2005). Reduced magnetization produced by increased methane flux at a gas hydrate vent. *Marine Geology*, *216*, 265–274. https://doi.org/10.1016/j.margeo.2005.02.027

Pandey, L., Sain, K., & Joshi, A. K. (2019). Estimate of gas hydrate saturations in the Krishna-Godavari basin, eastern continental margin of India, results of expedition NGHP-02. *Marine and Petroleum Geology*, *108*, 581–594. https://doi.org/10.1016/j.marpetgeo.2018.12.009

Passier, H. F., de Lange, G. J., & Dekkers, M. J. (2001). Magnetic properties and geochemistry of the active oxidation front and the youngest sapropel in the eastern Mediterranean Seafront and the youngest sapropel in the eastern Mediterranean Sea. *Geophysical Journal International*, *145*, 604–614. https://doi.org/10.1046/j.0956-540x.2001.01394.x

Passier, H. F., Middleburg, J. J., van Os, B. J., & de Lange, G. J. (1996). Diagenetic pyritization under eastern Mediterranean sapropels caused by downward sulphide diffusion. *Geochimica et Cosmochimica Acta*, *60*, 751–763. https://doi.org/10.1016/0016-7037(95)00419-X

Peketi, A., Mazumdar, A., Joao, H. M., Patil, D. J., Usapkar, A., & Dewangan, P. (2015). Coupled C–S–Fe geochemistry in a rapidly accumulating marine sedimentary system: Diagenetic and depositional implications. *Geochemistry, Geophysics, Geosystems*, *16*, 2865–2883. https://doi.org/10.1002/2015GC005754

Peketi, A., Mazumdar, A., Joshi, R. K., Patil, D. J., Srinivas, P. L., & Dayal, A. M. (2012). Tracing the Paleo sulfate-methane transition zones and $H_2S$ seepage events in marine sediments: An application of C-S-Mo systematics. *Geochemistry, Geophysics, Geosystems*, *13*, Q10007. https://doi.org/10.1029/2012/GC004288

Peketi, A., Mazumdar, A., Pillutla, S. P. K., Rai, V. K., Sawant, B., Chaitanya, A. V. S., & Krishna, R. (2020). Monsoon rainfall and contrasting source rocks influenced sediment composition of peninsular basins along the east coast of India (western Bay of Bengal). *Marine and Petroleum Geology*, *118*, 104433. https://doi.org/10.1016/j.marpetgeo.2020.104433

Peters, C., & Dekkers, M. J. (2003). Selected room temperature magnetic parameters as a function of mineralogy, concentration and grain size. *Physics and Chemistry of the Earth*, *28*, 659–667. https://doi.org/10.1016/S1474-7065(03)00120-7

Phillips, S. C., Johnson, J. E., Giosan, L., & Rose, K. (2014). Monsoon-influenced variation in productivity and lithogenic sediment flux since 110 ka in the offshore Mahanadi Basin, northern Bay of Bengal. *Marine and Petroleum Geology*, *58A*, 502–525. https://doi.org/10.1016/j.marpetgeo.2014.05.007

Phillips, S. C., Johnson, J. E., Miranda, E., & Disenhof, C. (2011). Improving CHN measurement in carbonate-rich marine sediments. *Limnology and Oceanography: Methods*, *9*, 194–203. https://doi.org/10.4319/lom.2011.9.194

Phillips, S. C., Johnson, J. E., Underwood, M. B., Guo, J., Giosan, K., & Rose, K. (2014). Long-timescale variation in bulk and clay mineral composition of Indian continental margin sediments in the Bay of Bengal, Arabian Sea, and Andaman Sea. *Marine and Petroleum Geology*, *58*, 117–138. https://doi.org/10.1016/j.marpetgeo.2014.06.018

Ponton, C., Giosan, L., Eglinton, T. I., Fuller, D. Q., Johnson, J. E., Kumar, P., & Collett, T. S. (2012). Holocene aridification of India. *Geophysical Research Letters*, *39*, L03704. https://doi.org/10.1029/2011GL050722

Poulton, S. W., Krom, M. D., & Raiswell, R. (2004). A revised scheme for the reactivity of iron (oxyhydr)oxide minerals towards dissolved sulfide. *Geochimica et Cosmochimica Acta*, *68*, 3703–3715. https://doi.org/10.1016/j.gca.2004.03.012

Powell, C. M., Roots, S. R., & Veevers, J. J. (1988). Pre-breakup continental extension in east Gondwanaland and the early opening of the eastern Indian Ocean. *Tectonophysics*, *155*, 261–283. https://doi.org/10.1016/0040-1951(88)90269-7

Radhakrishnamurty, C., & Subbarao, K. V. (1990). Palaeomagnetism and rock magnetism of the Deccan traps. *Proceedings of the Indian Academy of Sciences*, *99*, 669–680.

Ramana, M. V., Ramprasad, T., Paropkari, A. L., Borole, D. V., Rao, B. R., Karisiddaiah, S. M., et al. (2009). Multidisciplinary investigations exploring indicators of gas hydrate occurrence in the Krishna–Godavari Basin offshore, east coast of India. *Geo-Marine Letters*, *29*, 25–38. https://doi.org/10.1007/s00367-008-0121-7

Ramesh, R., & Subramanian, V. (1988). Temporal, spatial, and size variation in the sediment transport in the Krishna River Basin, India. *Journal of Hydrology*, *98*, 53–65. https://doi.org/10.1016/0022-1694(88)90205-3

Ramprasad, T., Dewangan, P., Ramana, M. V., Mazumdar, A., Karisiddaiah, S. M., Ramya, E. R., & Sriram, G. (2011). Evidence of slumping/sliding in Krishna-Godavari offshore basin due to gas/fluid movements. *Marine and Petroleum Geology*, *28*, 1806–1816. https://doi.org/10.1016/j.marpetgeo.2011.02.007

Rao, G. N. (2001). Sedimentation, stratigraphy, and petroleum potential of Krishna-Godavari basin, East Coast of India. *AAPG Bulletin*, *85*, 1623–1643. https://doi.org/10.1306/8626ccdf-173b-11d7-8645000102c1865d

Razik, S., Dekkers, M. J., & von Dobeneck, T. (2014). How environmental magnetism can enhance the interpretational value of grain-size analysis: A time-slice study on sediment export to the NW African margin in Heinrich Stadial 1 and Mid Holocene. *Palaeogeography, Palaeoclimatology, Palaeoecology*, *406*, 33–48. https://doi.org/10.1016/j.palaeo.2014.04.009

Rees, E. V. L., Priest, J. A., & Clayton, C. R. I. (2011). The structure of methane gas hydrate bearing sediments from the Krishna-Godavari Basin as seen from Micro-CT scanning. *Marine and Petroleum Geology*, *28*, 1283–1293. https://doi.org/10.1016/j.marpetgeo.2011.03.015

Riedinger, N., Pfeifer, K., Kasten, S., Garming, J. F. L., Vogt, C., & Hensen, C. (2005). Diagenetic alteration of magnetic signals by anaerobic oxidation of methane related to a change in sedimentation rate. *Geochimica et Cosmochimica Acta*, *69*, 4117–4126. https://doi.org/10.1016/j.gca.2005.02.004

Riedinger, N., Torres, M. E., Screaton, E., Solomon, E. A., Kutterolf, S., Schindlbeck-Belo, J., et al. (2019). Interplay of subduction tectonics, sedimentation, and carbon cycling. *Geochemistry, Geophysics, Geosystems*, *20*(11), 4939–4955. https://doi.org/10.1029/2019gc008613

Ritger, S., Carson, B., & Suess, E. (1987). Methane-derived authigenic carbonates formed by pore-water expulsion along the Oregon/Washington margin. *GSA Bulletin*, *98*, 147–156. https://doi.org/10.1130/0016-7606(1987)98<147:MACFBS>2.0.CO;2

Roberts, A. P. (2015). Magnetic mineral diagenesis. *Earth-Science Reviews*, *151*, 1–47. https://doi.org/10.1016/j.earscirev.2015.09.010

Rose, K. K., Johnson, J. E., Torres, M. E., Hong, W-L., Giosan, L., Solomon, E. A., et al. (2014). Anomalous porosity preservation and preferential accumulation of gas hydrate in the Andaman accretionary wedge, NGHP-01 site 17A. *Marine and Petroleum Geology*, *58A*, 99–116. https://doi.org/10.1016/j.marpetgeo.2014.04.009

Rowan, C. J., & Roberts, A. P. (2006). Magnetite dissolution, diachronous greigite formation, and secondary magnetizations from pyrite oxidation: Unravelling complex magnetizations in Neogene marine sediments from New Zealand. *Earth and Planetary Science Letters*, *241*, 119–137. https://doi.org/10.1016/j.epsl.2005.10.017

Sangode, S. J., Sinha, R., Phartiyal, B., Chauhan, O. S., Mazari, R. K., Bagati, T. N., et al. (2007). Environmental magnetic studies on some Quaternary sediments of varied depositional settings in the Indian sub-continent. *Quaternary International*, *159*(1), 102–118. https://doi.org/10.1016/j.quaint.2006.08.015

Schöbel, S., & de Wall, H. (2014). AMS-NRM interferences in the Deccan basalts: Toward an improved understanding of magnetic fabrics in flood basalts. *Journal of Geophysical Research: Solid Earth*, *119*(4), 2651–2678. https://doi.org/10.1002/2013jb010660

Shankar, U., & Riedel, M. (2014). Assessment of gas hydrate saturation in marine sediments from resistivity and compressional-wave velocity log measurements in the Mahanadi Basin, India. *Marine and Petroleum Geology*, *58A*, 265–277. https://doi.org/10.1016/j.marpetgeo.2013.10.007

Shukla, K. M., Collett, T. S., Kumar, P., Yadav, U. S., Boswell, R., Frye, M., et al. (2019). National Gas Hydrate Program Expedition 02: Identification of gas hydrate prospects in the Krishna-Godavari Basin, offshore India. *Marine and Petroleum Geology*, *108*, 167–184. https://doi.org/10.1016/j.marpetgeo.2018.11.013

Shukla, K. M., Kumar, P., & Yadav, U. S., & NGHP-02 Science team. (2019). Gas hydrate reservoir identification, delineation, and characterization in the Krishna-Godavari basin using subsurface geologic and geophysical data from the National Gas Hydrate Program 02 Expedition, offshore India. *Marine and Petroleum Geology*, *108*, 185–205. https://doi.org/10.1016/j.marpetgeo.2018.10.019

Solomon, E. A., Spivack, A. J., Kastner, M., Torres, M. E., & Robertson, G. (2014). Gas hydrate distribution and carbon sequestration through coupled microbial methanogenesis and silicate weathering in the Krishna–Godavari Basin, offshore India. *Marine and Petroleum Geology*, *58A*, 233–253. https://doi.org/10.1016/j.marpetgeo.2014.08.020

Southon, J., Kashgarian, M., Fontugne, M., Metivier, M., & Yim, W. W.-S. (2002). Marine reservoir corrections for the Indian Ocean and Southeast Asia. *Radiocarbon*, *44*, 167–180. https://doi.org/10.1017/S0033822200064778

Stern, L. A., & Lorenson, T. D. (2014). Grain-scale imaging and compositional characterization of cryo-preserved India NGHP 01 gas-hydrate-bearing cores. *Marine and Petroleum Geology*, *58A*, 206–222. https://doi.org/10.1016/j.marpetgeo.2014.07.027

Stuiver, M., Reimer, P. J., & Reimer, R. W. (2021). *CALIB 8.2*. Retrieved from http://calib.org

Subramanain, V. (1979). Chemical and suspended-sediment characteristics of rivers of India. *Journal of Hydrology*, *44*, 37–55. https://doi.org/10.1016/0022-1694(79)90145-8

Subramanian, V. (1980). Mineralogical input of suspended matter by Indian rivers into the adjacent areas of the Indian Ocean. *Marine Geology*, *36*, M29–M34. https://doi.org/10.1016/0025-3227(80)90084-5

Suits, N. S., & Arthur, M. A. (2000). Sulfur diagenesis and partitioning in Holocene Peru shelf and upper slope sediments. *Chemical Geology*, *163*, 219–234. https://doi.org/10.1016/s0009-2541(99)00114-x

Teichert, B. M. A., Johnson, J. E., Solomon, E. A., Giosan, L., Rose, K., Kocherla, M., et al. (2014). Composition and origin of authigenic carbonates in the Krishna-Godavari and Mahanadi Basins, eastern continental margin of India. *Marine and Petroleum Geology*, *58A*, 438–460. https://doi.org/10.1016/j.marpetgeo.2014.08.023

Torres, M. E., Hong, W. L., Solomon, E. A., Milliken, K., Kim, J. H., Sample, J. C., et al. (2020). Silicate weathering in anoxic marine sediment as a requirement for authigenic carbonate burial. *Earth-Science Reviews*, *200*, 102960. https://doi.org/10.1016/j.earscirev.2019.102960

Toyos, M. H., Lamy, F., Lange, C. B., Lembke-Jene, L., Saavedra-Pellitero, M., Esper, O., & Arz, H. W. (2020). Antarctic circumpolar current dynamics at the Pacific entrance to the Drake Passage over the past 1.3 million years. *Paleoceanography and Paleoclimatology*, *35*, e2019PA003773. https://doi.org/10.1029/2019PA003773

Usapkar, A., Dewangan, P., Badesab, F. K., Mazumdar, A., Ramprasad, T., Krishna, K. S., & Basavaiah, N. (2016). High resolution Holocene paleomagnetic secular variation records from Bay of Bengal, *Physics of the Earth and Planetary Interiors*, *252*, 49–76. https://doi.org/10.1016/j.pepi.2016.01.004

Usapkar, A., Dewangan, P., Kocherla, M., Ramprasad, T., Mazumdar, A., & Ramana, M. V. (2014). Enhanced methane flux event and sediment dispersal pattern in the Krishna-Godavari offshore basin: Evidences from rock magnetic techniques. *Marine and Petroleum Geology*, *58*, 461–475. https://doi.org/10.1016/j.marpetgeo.2014.08.008

Verosub, K. L., & Roberts, A. P. (1995). Environmental magnetism: Past, present, and future. *Journal of Geophysical Research*, *100*, 2175–2192. https://doi.org/10.1029/94JB02713

Weber, M. E., Lantzsch, H., Dekens, P., Das, S. K., Reilly, B. T., Martos, Y. M., et al. (2018). 200,000 years of monsoonal history recorded on the lower Bengal Fan - Strong response to insolation forcing. *Global and Planetary Change*, *166*, 107–119. https://doi.org/10.1016/j.gloplacha.2018.04.003

Wu, L., Wilson, D. J., Wang, R., Yin, X., Chen, Z., Xiao, W., & Huang, M. (2020). Evaluating Zr/Rb ratio from XRF scanning as an indicator of Grain-Size variations of glaciomarine sediments in the Southern Ocean. *Geochemistry, Geophysics, Geosystems*, *21*, e2020GC009350. https://doi.org/10.1029/2020GC009350